

**An Investigation into the Austenite Decomposition Behaviour and Post-Forming
Tempering Response of Two 1800 MPa Grades of Press Hardening Steels**

by

Claire Bourque

A Thesis

presented to

The University of Guelph

In partial fulfilment of requirements
for the degree of

Masters of Applied Science

in

Engineering

Guelph, Ontario, Canada

© Claire Bourque, December, 2019

ABSTRACT

AN INVESTIGATION INTO THE AUSTENITE DECOMPOSITION BEHAVIOUR AND POST FORMING TEMPERING RESPONSE OF TWO 1800 MPA PRESS HARDENING STEELS

Claire Bourque
University of Guelph, 2019

Advisor:
Dr. Alexander Bardelcik
Dr. Mary A. Wells

In this research, two different 1800 MPa grades of press-hardening steel were investigated; one with 0.30 wt% and the other 0.32 wt% of Carbon. The suitability of an austenite decomposition model after cooling and the effect of short tempering times after quenching on the final mechanical properties was examined. To assess the austenite decomposition model, both materials were subject to a variety of constant cooling and resulted in a mixed-phase of bainite, martensite, and ferrite. The Gleeble experiments were simulated using LS-Dyna and a thermal-mechanical-microstructural model. In the second investigation (Part II – Short Cycle Tempering), both steels were fully quenched in the Gleeble to produce a fully martensitic microstructure and tempered at temperatures ranging from 100 to 700 °C and times of 0.5 to 15 s. For both experiments microhardness tests were conducted on the specimens and a FESEM was used to characterize and quantify the resultant mixed-phase microstructures.

ACKNOWLEDGEMENTS

I would like to thank my advisors, Dr. Alexander Bardelcik and Dr. Mary A Wells for creating the opportunity for me to be apart of this project and to grow as a researcher.

I would like to thank the research group at the University of Waterloo, Ford Research USA, and Promatek Research Center for initiating and supporting this project. In particular I'd like to thank Constatin Chiriac for offering support and sharing has extensive knowledge of automotive steels.

I would like to acknowledge Dr. Hari Simha for his expertise and support during the period of my graduate studies.

I would also like to thank Mark Whitney, Massimo Di Ciano, Sante Di Cecco, and Eckhard Budziarek for the invaluable assistance they provided me in running my experiments and facilitating my use of the University of Waterloo labs.

Finally, I'd like to thank my parents and my brother for constantly motivating me and supporting my aspirations.

TABLE OF CONTENTS

ABSTRACT	ii
ACKNOWLEDGEMENTS.....	iii
TABLE OF CONTENTS	iv
LIST OF TABLES	vi
LIST OF FIGURES	vii
1 Background and Literature Review.....	1
1.1 Press Hardening of Boron Steels	1
1.1.2 Phase Transformation in Press Hardening Boron Steels	2
1.1.3. Effect of Microalloying Elements on Mechanical Properties in Press Hardening Boron Steels	4
1.1.4 Higher Carbon Press Hardening Steels.....	6
1.1.5 Intrinsic tailored blanks.....	8
1.1.6 FEA Simulation of Phase Decomposition	11
1.2 Martensite Tempering	12
1.2.1 Tempering of Martensite.....	13
1.2.2 Effects of alloying elements on Mechanical Properties During Tempering	15
1.2.3 Autotempering.....	18
1.2.4 Hardness testing.....	20
1.2.5 Rapid Tempering	21
1.3 Research Intent.....	27
1.3.1 Part I – Austenite Decomposition Model Optimization	27
1.3.2 Part II – Short Cycle Tempering	28
2. Experimental Methods.....	29

2.1 Materials and Equipment	29
2.1.1 High Carbon Ultra High Strength Press Hardening Steel.....	29
2.1.2 Equipment	31
2.2 Experimental Procedure	33
2.2.1 Gleeble Experimental Methodology.....	34
2.2.2 Specimen Preparation	39
2.2.3 Hardness Evaluation	40
2.2.4 SEM Microstructure Evaluation.....	41
2.2.5 LS-Dyna Simulation	42
3. Results and Discussion	44
3.1 Part I - Austenite Decomposition Model Optimization.....	44
3.1.1 Hardness Results	44
3.1.2 Microstructure Results	48
3.1.3 LS-Dyna Simulation Results.....	56
3.1.4 LS-Dyna Optimization.....	59
3.2 Part II - Short Cycle Tempering.....	63
3.2.1 Hardness Results	63
3.2.2 Microstructural Analysis.....	72
4 Conclusions and Recommendations	80
4.1 Conclusions.....	80
4.1.1 Part I – Austenite Decomposition Model Optimization	80
4.1.2 Short Cycle Tempering	81
4.2 Future Work.....	82
REFERENCES	83

LIST OF TABLES

Table 1: ICP analysis performed by Element Materials Technology on Steel A and B	30
Table 2: Steel A critical cooling rate hardness results	45
Table 3: Steel B critical cooling rate average hardness results	46
Table 4: Critical cooling rate microstructure average area phase results for Steel A	48
Table 5: Critical cooling rate microstructure average area phase results for Steel B.....	52
Table 6: The Measured (M) and Predicted (P) as-quenched microstructure constituents for Steel A	58
Table 7: The Measured (M) and Predicted (P) as-quenched microstructure constituents for Steel B	59
Table 8: The Measured (M) and Optimized Predictions (O) as-quenched microstructure constituents for Steel A.....	59
Table 9: The Measured (M) and Optimized Predictions (O) as-quenched microstructure constituents for Steel B	61

LIST OF FIGURES

Figure 1: Mechanical properties of 22MnB5 and CCT Diagram, adapted from [5].....	2
Figure 2: SEM micrographs of UHSS A (a-c) and UHSS B (dd-f) with cooling rates of 60 (a,d), 1 (b,e) and 0.01 °C/s (c,f)	5
Figure 3: (a) Microstructures for 1800 MPa sheet and (b) application to automobile bumper, adapted from [14].....	7
Figure 4: Flow diagram of blank tailoring strategies, adapted from [17].....	8
Figure 5: Die with segmented tools which include cartridge heaters and cooling channels to induce tailored quenching, adapted from [24]	10
Figure 6: The tailored and non-tailored axial crash members investigated by [27].....	11
Figure 7: SEM micrographs of auto-tempered material before and after deformation. (a) Before deformation. (b) After deformation. [50]	20
Figure 8: Inconsistent data in relation to low tempering temperature and time, adapted from [53]...	22
Figure 9: Schematic drawing of the microstructural evolution of heat treatable steel (a) after induction and (b) conventional hardening and (c) after induction and (d) conventional hardening and tempering. Adapted from [64]	26
Figure 10: Quench Profiles acquired from the Gleeble for steel A (right) and steel B (left)	36
Figure 11: In-Die heating simulation curves, adapted from Bardelcik et al. [33]	37
Figure 12: Gleeble Thermal-Mechanical Simulator.....	39
Figure 13: A post processed phase area quantification image with the original micrograph for	

comparison. The image pictured above is from TM2 for Steel A. The white is martensite (M), the red is bainite (B), the blue is ferrite (F), and the green in granular bainite (GB)	41
Figure 14: Critical cooling rate average hardness results and hardness standard deviation.....	44
Figure 15: Critical cooling rate average hardness results and hardness standard deviation.....	45
Figure 16: Average hardness results for Steel A and B.....	47
Figure 17: SEM micrographs for resulting quench conditions of 2.5 °C/s and 5 °C/s for Steel A	49
Figure 18: SEM micrographs for resulting quench conditions of 10 °C/s and 50 °C/s for Steel A	50
Figure 19: SEM micrographs for resulting quench conditions of TM1 and TM2 for Steel A	51
Figure 20: SEM micrographs for resulting quench conditions of 2.5 °C/s and 5 °C/s for Steel B	53
Figure 21: SEM micrographs for resulting quench conditions of 10 °C/s and 50 °C/s for Steel B ..	55
Figure 22: SEM micrographs for resulting quench conditions of TM1 and TM2 for Steel B	56
Figure 23: The average measured and predicted hardness for each quench rate for Steel A	61
Figure 24: The average measured and predicted hardness for each quench rate for Steel B	63
Figure 25: The resulting average hardness measurements for all tempering conditions and both hold times for Steel A.....	65
Figure 26: Heating and quenching profiles of the tempering cycle performed on Steel A for all temperatures and times	66
Figure 27: The resulting average hardness measurements for all tempering conditions and both hold times for Steel B.....	68
Figure 28: Heating and quenching profiles of the tempering cycle performed on Steel A for all temperatures and times	69
Figure 29: Average measured hardness for Steel A and Steel B. The figures a-e represent resulting	

hold times for both steels for the tempering times 0.5-15 s.....	71
Figure 30: Fully quenched microstructure for Steel A	73
Figure 31: SEM micrographs of sample tempered at 300 °C for Steel A	73
Figure 32: SEM micrographs of sample tempered at 500 °C for Steel A	74
Figure 33: SEM micrographs of sample tempered at 700 °C for Steel A	75
Figure 34: Fully quenched microstructure for Steel B	76
Figure 35: SEM micrographs of sample tempered at 300 °C for Steel B.....	77
Figure 36: SEM micrographs of sample tempered at 500 °C for Steel B.....	78
Figure 37: SEM micrographs of sample tempered at 700 °C for Steel B.....	79

1 Background and Literature Review

1.1 Press Hardening of Boron Steels

Press hardening of 22MnB5 steel is a mature and widely accepted metal forming technology that is used to reduce vehicle weight while maintaining occupant protection during a crash. Press hardened parts can produce as-formed components with tensile strengths of 1500 MPa and greater. These press hardened parts are mainly used as reinforcement members within a vehicle body-in-white (BIW) structure. [1]. The demand for increased fuel economy has led to vehicle design with increasingly lower volumes of steel. The structural integrity of the vehicle must be maintained, and to supplement this decrease in steel use, research into high and ultra high strength steel development has been motivated. Lower strength conventional steels are being replaced with higher strength advanced high strength steels in vehicle structural applications [2].

Press hardening was first developed by a Swedish Company, Plannja, and was used to create saw and lawn mower blades [3]. Some of the first press hardened parts in commercial vehicles were developed by Saab Automobile Ab. The implementation began around the late 1990s, with much expansion in the field occurring in the late 2000s [4]. Press hardening can be divided into two different techniques, one being direct press hardening and the other being indirect press hardening. In direct press hardening, a blank is austenitized in a furnace before being transferred to a cold die, where it is simultaneously formed and quenched. In indirect press hardening, a part is cold formed to near final geometry, then it is austenitized and subject to a quenching and calibration operation within a cold die. The main objective in press hardening is to increase the tensile strength of the steel by

inducing a full martensitic transformation in the part. Figure 1 shows different steel types and compares the elongation versus the tensile strength.

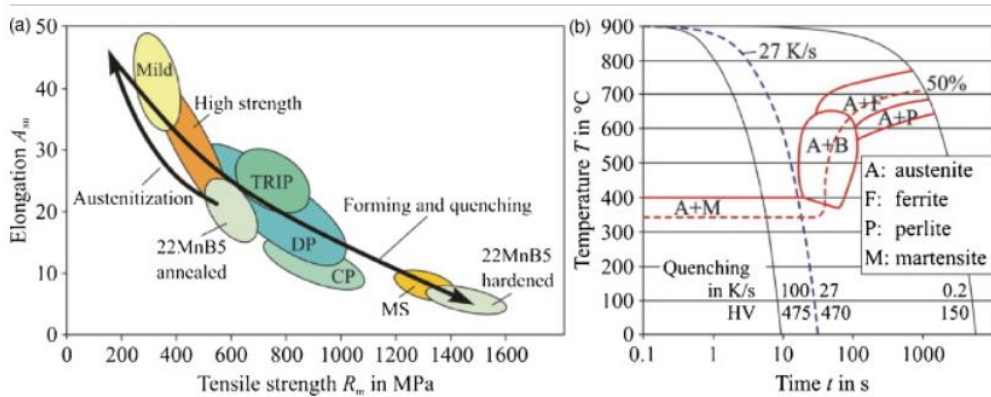


Figure 1: Mechanical properties of 22MnB5 and CCT Diagram, adapted from [5]

Boron steel is the most commonly used press hardening material. The most common grade of boron steel is 22MnB5, which results in an as-formed tensile strength of 1500 MPa. This steel has the ability to quench harden, which greatly improves the tensile strength by allowing a fully martensitic phase transformation at moderate quench rates. The strength increase through quenching is done by heating this material to a temperature above the A_{c3} and holding it for a sufficient amount of time to austenitize the steel and then quenching to room temperature at a rates greater than 30 °C/s within the die as shown by the continuous cooling transformation (CCT) diagram for 22MnB5 in Figure 1. The final part created after quenching has high strength due to the martensitic microstructure and is therefore very effective when used for intrusion protection within the Body in WHITE [6].

1.1.2 Phase Transformation in Press Hardening Boron Steels

Three different kinds of phase transformations exist; diffusion-dependent with no change in phase composition or number of phases presents, diffusion-dependent with changes in phase compositions or number of phases, and diffusionless phase transformation where metastable phases are produced.

Quenching of heat treatable boron steel involves the diffusionless transformation of austenite into martensite. The critical cooling rate is the minimum rate of continuous cooling required for the diffusionless transformation of austenite to martensite. [7]

Austenite is the face-centered-cubic (FCC, gamma iron) phase and is not stable below the eutectoid temperatures unless cooled rapidly. The critical temperatures range for hypoeutectoid steels are between A_{c1} and A_{c3} , known as the intercritical temperatures. Between these temperatures the alloy exists as austenite and ferrite. Steel must be heated above A_{c3} in order for the entire microstructure to transform into austenite, after which quenching can occur to transform the microstructure from austenite into the other phases. Ferrite is a body-centered-cubic (BCC, alpha or delta iron) form of iron. Alpha ferrite is stable at room temperatures and transforms into austenite at high temperatures. Delta ferrite has the same structure as alpha ferrite and is stable at high temperatures. Alpha ferrite forms from slow cooling of austenite and is caused by the rejection of carbon by diffusion.

When steel with a carbon content of at least 0.5% w.t. is heated to 815 °C with sufficient holding time, the carbon will be dissolved in the interstices of the FCC crystal. If cooling is slow enough, the transformation from FCC to BCC of the crystal begins. This begins to occur when temperatures drop below the A_{c3} . Carbon atoms have minimum solubility in the ferrite or alpha crystal lattice and during slow cooling the alloy returns to its equilibrium state in terms of the phases present. Magnetic changes occur at 770 °C when iron carbon alloy is converted to austenite by heat, and a large absorption of heat occurs at the transformation temperature. [8]

M_s is the martensite start temperatures where martensite begins to transform and continues during cooling until the martensite finish temperature (M_f) is reached. When the alloy is cooled rapidly carbon atoms cannot escape from the iron lattice. This results in a distortion of the lattice, and if

cooling is fast enough martensite is formed. This structure is an aggregate of iron and cementite and is an alpha phase. The austenite to martensite transition does not involve diffusion and no thermal activation is needed. Martensite forms nearly instantaneously when the required low temperature is reached. The FCC gamma austenite transforms into a BCT unit cell. Martensite is metastable and is unreactive at room temperature. [9] [8]

Bainite is formed at cooling rates slower than that for martensite formation and faster for that of ferrite and pearlite. Two kinds of bainite exist, upper and lower bainite. Upper bainite generally forms at temperatures between 550 and 400 °C. When the carbon concentration in the austenite is high enough, cementite nucleates as discrete particles or discontinuous stringers at ferrite/austenite interfaces. As the carbon content increases, the cementite filaments can become more continuous. At very high carbon contents, the bainitic ferrite laths are finer with the cementite stringers more frequent and continuous which can be described as 'feathery' bainite. Lower bainite generally forms at temperatures between 400 and 250 °C and the precise changeover temperature between upper and lower bainite depends on carbon content in steel. [10]

1.1.3. Effect of Microalloying Elements on Mechanical Properties in Press Hardening Boron Steels

The final properties of the steel after press hardening are mainly dependant on the carbon content. By increasing the carbon content, the strength of the material can be improved, but the ductility will also decrease. Alloying elements such as Mn and Cr have a small influence on the strength of the material after quenching. The main affect of these elements is on increasing the hardenability of the steel [6]. Boron is another element which influences hardenability as it retards the transformation of eutectoid phases from austenite, by “poisoning” the nucleation sites for these phases at the austenite grain

boundaries. This has an effect of pushing the bainite window CCT diagram towards the right as shown in Figure 1. Other alloying elements include Co, Si, Ni, Mo, and W. These alloying elements play a roll in enhancing strength and hardenability through transformation strengthening. Combined with carbon, these elements can aid in increasing the hardness of a stamped steel [2].

In work by Ali et al. [10] the influence of C, Cr, and Ni were evaluated with respect to cooling rate. Mechanical properties of different steels with varying levels of C, Cr, and Ni cooled at 60, 1 and 0.01 °C/s were evaluated. It was found that higher contents of C and Cr showed lower transformation temperatures than steel with higher Ni content as well as reduced grain and lath size. The results of cooling at three different cooling rates for the two different alloyed UHSS can be seen in Figure 2.

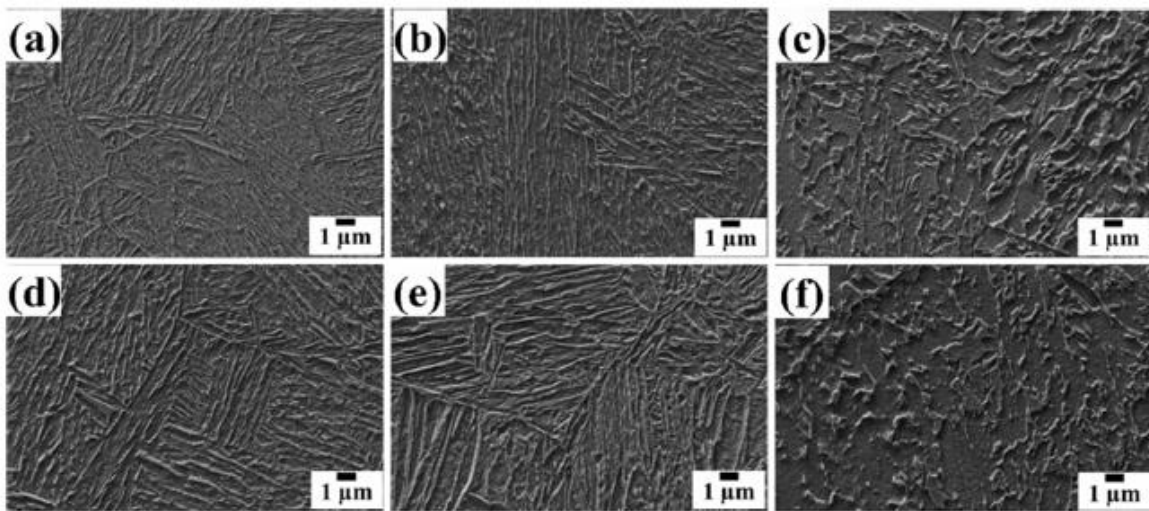


Figure 2: SEM micrographs of UHSS A (a-c) and UHSS B (d-f) with cooling rates of 60 (a,d), 1 (b,e) and 0.01 °C/s (c,f)

Jarvien et al. [11] studied the role of Ti and V when combined with Cr and Mo in UHSS press hardening steels. The microstructure properties were analyzed after die quenching and a bake hardening heat treatment. It was found that Ti and V could provide grain size refinement by forming stable nanosized precipitates. Improvements in bendability were confined to two V-microalloyed

steels that lacked Al-Ti-B additions. The conclusions made were that combining V with either Cr or Mo, improved mechanical properties in this experiment.

1.1.4 Higher Carbon Press Hardening Steels

Developments in vehicle light-weighting have led to implementation of press hardened 1800 MPa grades of steels within vehicle BIW structures. In an 1800 MPa boron steel, the improved strength is a direct correlation to increased carbon content [12].

Tokizawa et al. [13] proved that adding Ti content to 22MnB5 may increase the tensile strength and combined with rapid, low temperatures can create steel grades with tensile strengths up to 2000 MPa were achieved. In this same study, they concluded that conventional 22MnB5 press hardening process parameters can be used to produce 1800 MPa grades of press hardened parts.

In research performed by Hikida et al. [14], the tensile strength and toughness of 22MnB5 was improved by increasing the carbon content and refining the prior austenite grains. The resulting microstructure had smaller austenite and martensite grains compared with conventional sheets. The change in austenite and martensite grain size can be seen in Figure 3 where the conventional and developed steels are compared.

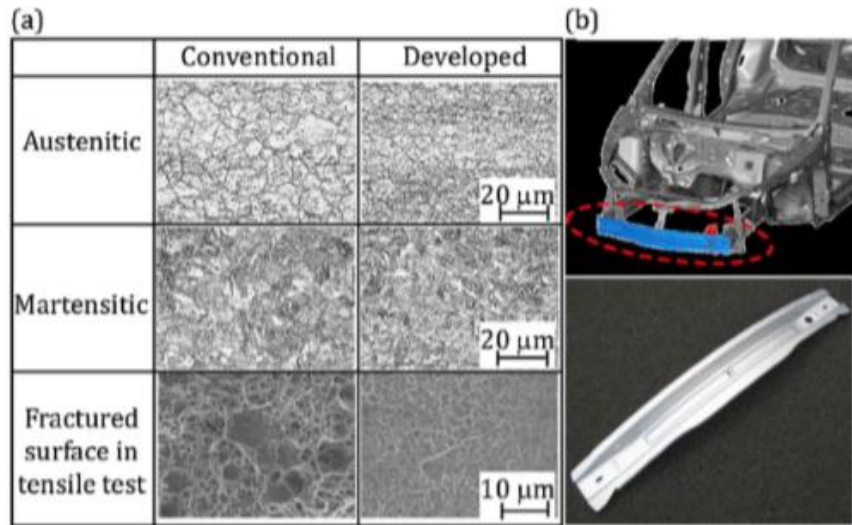


Figure 3: (a) Microstructures for 1800 MPa sheet and (b) application to automobile bumper, adapted from [14].

Yi et al. [15] were able to increase the tensile strength of a boron steel to 1880 MPa while maintaining 16% elongation by using a steel with a carbon content between 0.2 and 0.4 wt.%. The Mn content of this steel was also between 5 and 8 wt.%, giving the material an austenitization temperature between 790 and 840 °C.

For a 2000 MPa grade of press hardening steel, Taylor et al. [16] found that a high quench rate resulted in a complete martensite transformation within 1.5 s. They found that this also correlated the lath size to increased strength for a 38MnB5 steel, which also showed greater microstructural homogeneity when compared to 22MnB5.

1.1.5 Intrinsic tailored blanks

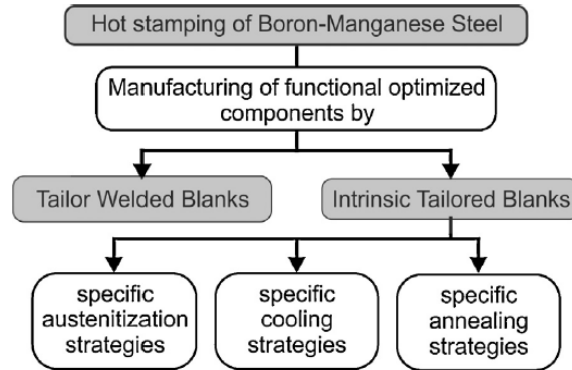


Figure 4: Flow diagram of blank tailoring strategies, adapted from [17]

Intrinsic tailoring of blanks can be performed during the heating and/or cooling of a press hardening process. Blank tailoring can be used to add ductility into a structural component for improved crash worthiness by controlling the heating and cooling parameters. Having areas of lower strength and greater ductility on a B-pillar has been proven to improve energy absorption. In Figure 4, intrinsic tailored blanks can be seen in the third row of the flow diagram, below “Manufacturing of functional optimized components” and beside “Tailor Welded Blanks”. Tekkaya et al. [18] examined the partial austenitization strategies which can occur during the heating of the steel in the press hardening process. Specific areas of the sheet metal were kept at lower temperatures to prevent martensitic microstructure development while other parts were kept above the austenitization temperature. During cooling, the die can be used to change the cooling rate on the surface of the blank. These tailoring procedures can be performed with a locally heated tool as seen in a study by Bardelcik et al. [19] or a blank as seen in a study by Liang et al. [20]. These processes can be used to influence the cooling rate to change the volume phase fraction produced when austenite is slow cooled to room temperature.

1.1.5.1 Tailor Die Quenching

Tailored die quenching is the procedure in which the time-temperature profile of a blank during forming and quenching is controlled by regulating the cooling conditions and the heat transfer from the die to the blank. A small temperature difference between the die and the blank can result in a slower cooling rate and the development of a different microstructure. Mori et al. [21] analyzed tailor die quenching's ability to produce sheets of UHSS with strength distribution. Local portions of the heated sheet were quenched by holding grooved tools at the bottom of the blank during stamping. The grooving tool created non-contact areas and the strength in the contact portions were therefore higher due to the quenching. In another study by Mori et al. [22] by pass resistance heating was used to heat the blank to various temperatures. A hat shaped part with a hardness of 500 HV20 around the corners and 280 HV20 everywhere else was formed.

In research done by Oldenburg et al. [23] tools were heated and cooled to use this effect and regulate the heat transfer from the blank to the tools. This resulted in varying microstructures with different mechanical properties. Channels can also be cut into the tool surface to create an air gap between the blank and tool to reduce the corresponding heat transfer coefficient. This was modelled by George et al. [24] and the resulting mechanical properties simulated. This method only works for indirect hot stamping. Images of the die with cooling channels included can be seen in Figure 5.

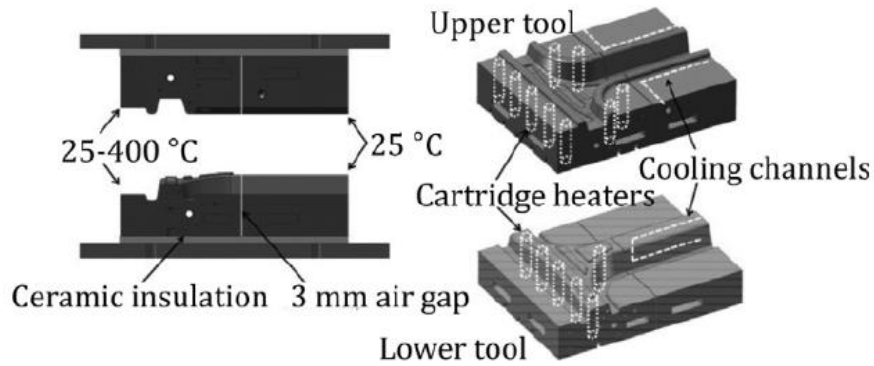


Figure 5: Die with segmented tools which include cartridge heaters and cooling channels to induce tailored quenching, adapted from [24]

In research done by Prajogo [25] in-die heating was used to locally modify quench rates and therefore the resulting microstructure to produced tailored properties in a top hat cross-section side impact beam. This work was later modified for a thesis and numerical simulations of a three-point bend experiment using LS-Dyna of this part were simulated and used to predict the crash performance of the beams [26].

In research conducted by Omer et al. [27], four configurations of tailored hot stamping conditions were created where the tool was partitioned into zones what were either heated or cooled. This method proved to create tailored microstructures on an axial crash member, confirmed using Vickers hardness measurements. Using the Akerstrom material model in LS-Dyna to predict the final hardness of the model was predicted and compared with the fabricated parts. The four tailoring configuration of the axial crash members can be seen in Figure 5.

Field et al. [28] used direct contact heating to produce a part where the microstructure was precisely controlled. This was mainly possible due to the different thermal effusivity of steel and ceramic regions on the heating die. The final part produces had a mixed ferrite/ martensite microstructure.

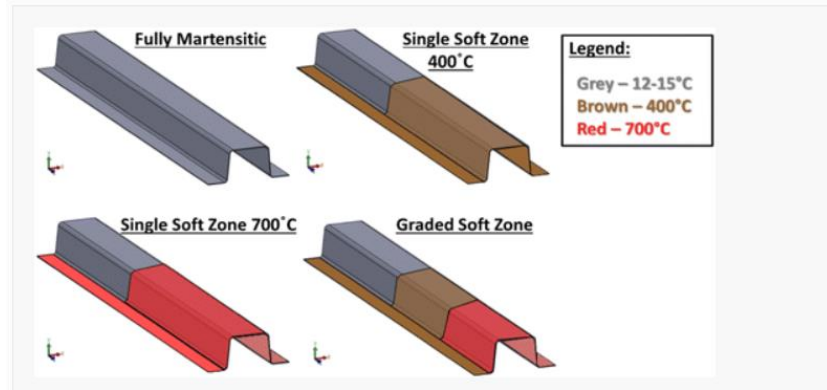


Figure 6: The tailored and non-tailored axial crash members investigated by [27]

1.1.6 FEA Simulation of Phase Decomposition

It is now commonplace to simulate press hardening operations using finite element (FE) analysis.

These FE models utilize coupled thermal-mechanical-microstructural constitutive models, which can predict austenite decomposition based on steel composition. One such model, *MAT_244 (*MAT_UHS_STEEL) within the commercial FE code LS-Dyna. This model is based on Kirkaldy's rate equations [29] and was implemented by Akerstrom and Oldenburg [30]. The model was adjusted for the addition of Boron by [30] to better simulate phase decomposition during press hardening of boron steels. This model has been successfully used and calibrated to predict the sub-critical cooling rate phase transformations for 22MnB5 by a number of authors [30] [31] [32]. In the work mentioned previously by ref [27], the activation energies in this card were optimized using LS-Opt to better predict the final phases and hardness.

The Kirkaldy rate equation states that the rate at which austenite decomposes into martensite is based on the effect of the alloy composition $f(C)$, the effect of the temperature $f(T)$, the effect of the current fraction formed, $f(X_i)$, the effect of the austenite grain size $f(G)$. In the function for the

effect of current fraction formed, X_i represented the fraction of the phases for bainite, austenite, pearlite, and ferrite.

$$\frac{dX_i}{dt} = f(G)f(C)f(T)f(X_i)$$

The function $f(T)$ is affected by the activation energy Q_i , which is a parameter that can be adjusted to change the resulting volume phase fraction in LS-Dyna and was done so by [27].

$$f(T) = (T_{cr} - T)^n e^{-Q_i/RT}$$

As part of research in [28], an FEM model was produced to simulate the measured results and the simulation used empirical first-order austenitization models developed from constant heating rate dilatometry measurements carried out in a Gleeble Thermal Mechanical Simulator 3500. This information was used to simulate the phase hardness of the final material. Bardelcik et al. [33] simulated the in-die quenching of a blank using a Gleeble Thermal Mechanical Simulator 3500 to investigate deformation during press hardening. The heating profiles used in the Gleeble experiments were imposed in LS-Dyna to model phase decomposition.

1.2 Martensite Tempering

Martensite is a very hard phase with a high yield and tensile strength but low ductility. Tempering is a heat treatment that can be used to improve the ductility and toughness of a press hardened steel part at the expense of the material strength. The purpose of tempering a press hardened high strength steel is to improve the toughness of the material. Improved toughness can be represented through increased elongation, improved yield strength, and decreased hardness. These improvements allow the high strength steel to absorb more energy during a crash situation and is very applicable to automobile

body-in-white (BIW) structural components. In Figure 4, martensitic tempering can be found in the last row of the flow diagram under specific annealing strategies.

High Strength Steels (HSS) and Advanced High Strength steels (AHSS) can be composed of a number of phases. These are martensite, ferrite, bainite, and retained austenite. Press hardened steels are considered Ultra High Strength Steels (UHSS) due to their fully martensitic microstructure. Press hardened parts benefit from high strength, minimal springback, but reduced ductility when compared to their cold formed counterparts. For vehicle crash applications, the fully martensitic parts could benefit from local areas where ductility is improved. One such method of introducing softer regions is to temper the martensite by heating the martensite and causing the transformation of martensite into tempered martensite, which has a lower strength, but higher ductility and toughness [34] [35] [6].

1.2.1 Tempering of Martensite

Tempering occurs when martensite and possibly retained austenite microstructures are heated to temperatures below the A_{c3} . Untempered martensite is super saturated with carbon in iron, making these microstructures unstable at higher temperatures and begin to decompose when heated. Carbon atoms are ejected from the supersaturated martensitic phase creating tempered martensite, ferrite, and carbide precipitates. This is realized through heating to a temperature below the eutectoid temperature (730°C) for a sufficient period of time. Tempering can be carried out isothermally at temperatures from $250\text{-}650^{\circ}\text{C}$. Tempered martensite, α -carbide, and cementite are by-products of tempering. Light and electron microscopy have been used to observe four separate stages of tempering. Each different stage of tempering has an impact on the final microstructure of the tempered material [35] [36].

1.2.1.1 Stage I Carbon Segregation

Between 80-200°C, the segregation and redistribution of carbon atoms takes place into lattice defects [35]. These defects can include dislocations, lath boundaries, and prior γ grain boundaries. These sites are all lower energy. Around 90% of the carbon is redistributed during the material cooling below the M_s temperature with a carbon content of 0.2%. Above 0.2% C, the carbon can be held in defect free regions. Transitional ε -carbides (ε -Fe_{2.4}C) can also begin to form at temperatures as low as 100°C [37].

1.2.1.2 Stage II Carbide Precipitation

Temperatures during this stage can range from 200-300°C. Extremely small spherical carbide particles become uniformly distributed when the steel contains more than 0.2% C. ε -carbide can also form producing orthorhombic structures isomorphous with transition metal carbides of the M_2C type (M can represent a number of alloying elements). This phase is eta carbide. Cementite, Fe₃C, transforms at temperatures above 250°C and is also known as theta carbide. The cementites create lath-like platelets which later form spheroidal particles that rapidly coarsen at higher temperatures. These cementite particles are mostly located at the boundaries of ferrite grains formed by recovery or recrystallization of the martensite grain boundary. Cementite, due to its orthorhombic shape can cause tempered martensite embrittlement [38].

At lower temperatures the carbide particles can appear plate shaped. Carbide formed at higher temperatures is more spheroidal in shape, these particles can be seen to decrease in size and increase in number with increased tempering temperature and time [7] [39].

1.2.1.3 Stage III Decomposition of Retained Austenite

At temperatures between 250-350°C, the interlath film like retained austenite decomposes into ferrite and cementite. This only occurs after the transitional carbides (η -carbide, ε -carbide) are well established [7].

1.2.1.4 Stage IV Recovery and Recrystallization

The defects of the martensite microstructure begin to recover, and cementite begins to form a coarse, spheroidal structure. At temperatures between 350-600°C. The decrease in carbon content in the martensite as well as the annihilation of grain boundaries and random dislocations results in formation of ferrite. The ferrite grains grow with further tempering with a plate like appearance. Cementite spheroidizes and coarsens unless certain steps are taken to avoid this [40]. And recrystallization of the ferrite matrix can occur at 600-700°C. Around these temperatures alloy carbides also begin to form. The higher the carbon content of the steel, the less rapid the recovery of the matrix occurs. This is due to the carbide particles inhibiting the migration of the grain boundaries [38]. The general trend of martensite softening as tempering temperatures increase is likely due to the recovery and recrystallization of martensite which begins to transform into equi-axed ferritic grains as carbides precipitate out of the metastable martensitic microstructure [35].

1.2.2 Effects of alloying elements on Mechanical Properties During Tempering

Adding alloying components to steels has proven to increase the stability of different phases, most notably austenite. The alloying elements can also slow the diffusion of carbides to maintain some hardness in materials. Different alloyed steels and processes have been used to optimize the final results of the tempering process.

Alloying elements such as manganese (Mn) have been found to delay the growth of cementite particles during later stages of tempering due to Mn partitioning between cementite particles and martensite [41].

Nickel decreases the ductile-to-brittle transition temperature by promotion of a cross-slip of dislocations in the ferritic as well as martensitic structures [44]. In a study by Krawczyk et al. [45], an increase in nickel content in structural steels was found to decrease ε -carbide concentration after tempering at 200 °C. The impact resistance of the steel with higher Ni content increased, which was found to be caused by nickel hindering nucleation of M_3C carbides.

Silicon (Si) and Aluminum (Al) are also used to suppress precipitation of cementite during tempering process. Silicon plays a larger role in retained austenite stabilization and is used often in high carbon TRIP steels [46]. Aluminum also plays a role in density reduction and solid strengthening. Niobium (Nb) and copper (Cu) strengthen the matrix using the precipitation strengthening affect and combine with nearby iron or carbon.

Tempering needs to be used to make full use of the precipitation effect of Nb and Cu in alloyed steels. Niobium can refine the microstructure by slowing down the austenite recrystallization and can strengthen the matrix by forming nano-sized carbide precipitates (precipitate strengthening affect). Molybdenum (Mb) is added to help strengthen the precipitates and the solution. The precipitates such as ε -Cu can generally inhibit the recovery of the dislocations by the pinning effect. This in turn can

slow down the effects of decomposition and can slow down the softening of the microstructure. Copper also has a significant precipitation strengthening effect by the formation of FCC ϵ -Cu precipitates when aging at temperatures between 500-700°C [47].

1.2.1.5 Carbide Precipitation

Epsilon carbide precipitation in steel martensite can occur in the first stage of tempering initiation. These carbides can be found within the laths during quenching for steels with lower M_s temperatures. Around temperatures as low as 80°C, ϵ -carbides, a transitional carbide phase, can form cementite. These carbide particles nucleate in the closely spaced defects, creating needle shaped precipitates at certain temperatures. These particles grow larger and become rod shaped at increased times and temperatures. These rods can also later form into a more disk-like shape [34] [48].

Distribution of coarse carbides can introduce brittle fracture modes [7]. The distance between carbides can be a determining factor in affecting material toughness. Increased temperatures are found to decrease carbide critical size and therefore fracture at these sites. Carbides in the form M_3C should be suppressed to reduce the effects of embrittlement. Fracture can occur along grain boundaries and carbides due differences in hardness, a negative effect of secondary hardening during tempering. The formation of needle like carbides have been shown to possibly increase toughness of a material where rod-like ϵ -carbide can dramatically worsen overall properties [48] [49].

Understanding carbide precipitation is very important when trying to increase the toughness of a steel due to the brittle fracture mode coarse cementite can create. The addition of Si can help to suppress formation of ϵ -carbides during low temperature tempering. Silicon can also delay transformation of ϵ -carbides to cementite. This was seen by Ju et al. [40] in their research. Other alloys such as Mo and Cr combine with existing carbides and slow the softening through the cementite precipitation growth.

Controlling the carbide precipitation can help to create steels with higher or lower hardness after tempering. Fine carbides can precipitate in the martensite matrix during tempering at 425°C for 30s [49].

Cementite, or iron carbide, is a transition metal carbide with the formula Fe_3C . It has an orthorhombic crystal structure and is hard and brittle. In carbon steel, as austenite transforms into ferrite, cementite is produced, or from martensite during tempering. Cementite can increase strength but decrease toughness as it is very hard and brittle. Cementite adds to the secondary hardening in the tempering processes.

The addition of substitutional Si atoms (~ 2 wt%) has proven to be able to modify the tempering characteristics of martensite. Si acts as a barrier for cementite growth due to the diffusion of Si within the ferrite matrix and the further enrichment of interface ferrite-cementite in the later stages of tempering. Steel with a large amount of Si that has been tempered finds an increased amount of ϵ -carbides in the matrix compared with other precipitate. Two conditions influence the affect Si has on the rate of cementite precipitation; the amount of Si the cementite inherits from the parent phase, and the presence of dislocations which reduce the available carbon content for precipitation and growth [46].

1.2.3 Autotempering

Autotempering occurs during the quenching process. The martensitic transformation begins at M_s and finishes at the M_f temperatures. These two temperatures ranging between 400°C and 250°C respectively. Tempering occurs when the first martensite forms just below the M_s temperature and is subject to a high enough temperature and a slow cooling rate. The release of the latent heat of

martensite causes transformation at the M_s temperature. This leads to the development of autotempered martensite during quenching or cooling. Autotempering was not found to adversely affect the fully hardened properties of the final steel product. In a study by Matsuda et al. [50], the change in adding Cr and B to a martensitic steel in relation to autotempering was examined. The steel was heated to 1093 K, held for 180 s and cooled at 10 K/s to 773K and held for another 90 s before cooling to room temperature at a rate of 10 K/s. The tensile strength increased from 1050 MPa to 1180MPa due to this addition of different alloys. In this study the hardness of martensite was found to be dependant on the M_s temperature. Matsuda et al. found that increasing the carbon content can lower the M_s temperature. This can lead to the decrease in the hole expansion ratio with increasing tensile strength. The addition of Cr and B allowed the M_s to remain high, improving the hole expansion ratio and increasing the softening. Higher M_s leads to auto-tempering during the cooling after martensitic transformation, and to a decrease in the difference of hardness between the ferrite and martensite. Hardness variations of martensite in well tempered steels through auto-tempering may contribute to an improvement in ductility and may decrease workhardening. In Figure 7, SEM micrographs of well tempered and less tempered martensite are presented for comparison. In work conducted by Jarvinen et al. [51], the effect of the paint baking treatment of 170 °C for 20 mins on 30MnB5 and 34MnB5 was studied. They found carbide rich regions within martensite lath to be evidence of auto-tempered martensite within the microstructure. In later work produced by Jarvinen et al. [11], a paint bake cycle was applied to five differently microalloyed 34MnB5 steels. The bake hardening treatment improved the postuniform elongation values, which was concluded to show a trend of improved ductility.

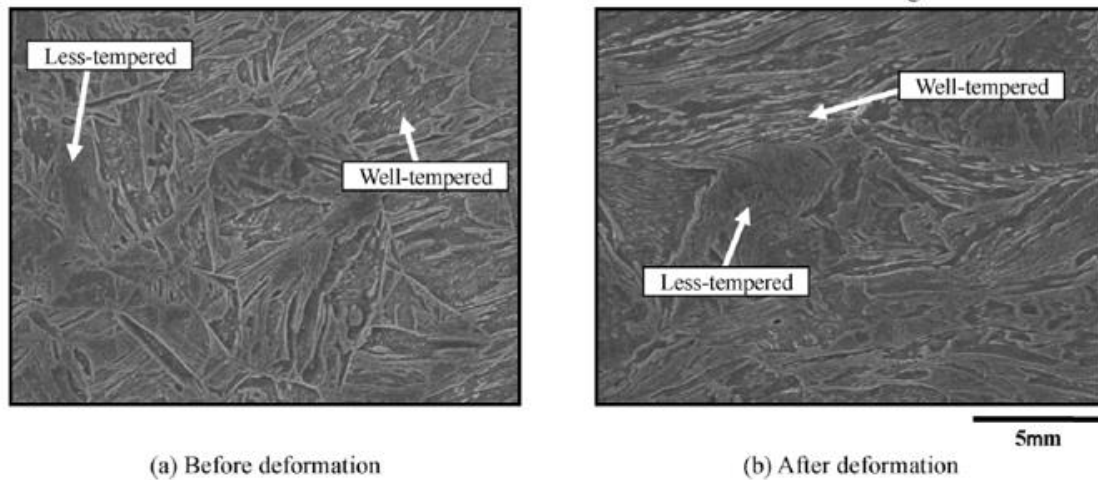


Figure 7: SEM micrographs of auto-tempered material before and after deformation. (a) Before deformation. (b) After deformation. [50]

1.2.4 Hardness testing

Hardness testing can be performed to determine steel softening during tempering. This can help to support microstructure findings and determine relationships between tempering time and temperature and resulting hardness. Hardness testing can give some insight into the material's mechanical properties [52]. Lu et. al [53] approximated the hardness of the welded area using the JMAK equation. Resistance spot welding was used in this case; therefore this was a non-isothermal process. The JMAK equation was then modified based on the additive rule. The minimum hardness (H_{∞}) due to complete tempering of martensite was determined by a heat treatment of base metal at 650 °C for 1 h in a conventional furnace. Vickers hardness was measured along the centerline of the tested coupon with a load of 500g. Ten hardness measurements were taken for each tempering condition tested. Vickers microhardness measurements were found in a number of other tempering studies using loads from 200g-1kg and dwell times of 15s. The amount of Vickers measurements taken ranged

from 12-25 [54] [55] [56] [37] [57] [46] [40]. Ju et al. [40] made a note of taking indents 3 mm away from the sample edge to avoid any decarburisation from the heat treatments.

1.2.5 Rapid Tempering

1.2.4.1 Resistance Spot Welding

Resistance spot welding, due to the heating of the microstructure in a specific area to a high temperature for short amounts of time, can cause tempering. The effects of tempering during spot welding has been studied to quantify the extent to which the microstructure softens. The observations made from the resulting tempered microstructures of resistance spot welding gave insight into the possibility of tempering to be used as a tailoring treatment. Baltazar Hernandez et. al [55] used resistance spot welding to characterize non-isothermal tempering of dual phase steel and study effects tempering had on the carbide precipitation. The effects on hardness of isothermal and nonisothermal process were also compared. Each specimen tested was tempered at 650°C using a resistance spot welder. The rapid tempering caused diffusion of carbon atoms into lath boundaries, grain boundaries, block boundaries, and dislocations, creating the dominant precipitate of cementite. The precipitated cementite in the non-isothermal tempering created Fe₃C, Mn₃C, and Cr₃C type carbides. The effect of the increased Cr and Mn content played a role in softening. The fine cementite and additional alloys led to decreased softening in comparison with the lean martensite structures. The non-isothermal tempering resulted in a hardness drop of about 30 HV and the isothermal tempering a higher hardness drop of 78 HV and 118 HV was measured for tempering held for 300 and 5400 seconds.

Lu et. al [53] modelled the non-uniform temperature gradients experienced during RSW leading to the subcritical HAZ. The model was able to predict surface electrode indentation, nugget size and local hardness. A 3-D coupled electro-thermo-mechanical model incorporating an improved electrical

contact resistance formula was developed for use during welding on an AISi coated hot stamped boron steel which accurately predict the local sub-critical HAZ softening. The A_{C1} and A_{C3} were found using a Gleeble and were chosen to be between 350-650°C. The tempering time ranged from 0.2-10s. It was found the softening kinetics at low temperatures occur more slowly. The hardness was reduced by 8.7% when tempered at 350°C for 10s, while during high tempering temperatures the hardness dropped in the sub critical HAZ by 37. Overall, the predicted value corresponded well with the experimental data, especially at high tempering temperatures. It was found in another study by Biro et al. [58] that carbide nucleation in M220 steel was very fast and could be observed at low temperatures for short tempering times as represented in the data by Lu et. al and demonstrated by the poor fit for data points at low temperatures and short times, as seen in Figure 8.

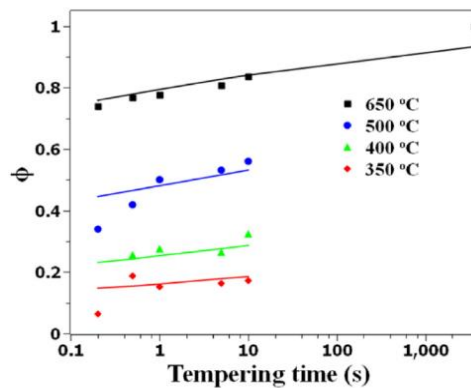


Figure 8: Inconsistent data in relation to low tempering temperature and time, adapted from [53]

1.2.4.2 Laser Tempering Effects on Microstructure

Laser welding is the process of joining parts where the energy source to melt the materials being joined is the laser beam. Tempering occurs during laser welding which alters mechanical properties of the resulting part. Laser welding can produce local heating below the melting temperature of the steel and can result in lower hardness and increased ductility.

In a paper by Gunnardottir and Basurto [59], 22MnB5 press hardening steel was induction tempered to soften the microstructure and allow for self-piercing rivet application. Self-piercing rivets can be used as a mechanical fastening process for joining sheet metals. To pierce the boron steel, it has to be first softened locally with a laser which causes deformation. The softening of the microstructure decreased in similar magnitudes and were within an average of 20 Vickers hardness measurements for each corresponding temperature compared with the data collected during these experiments. The four temperatures were (492, 684, 745, and 798 °C) and a tempering hold of 0.5 s.

Zhang et. al [56] analyzed the microstructural changes in the HAZ and fusion zone of a FLW on DP980 steel at 6kW. They used a Gleeble to validate these results in the HAZ and fusion zone. A heating rate of 200°C/s, with peak temperatures of 373K to 1473K and holds of 0.5 s before water quenching. The most relevant phase transitions induced by the FLW included the formation of new martensite grains in the upper-critical HAZ and fusion zone. There were two softened zones in the sub-critical HAZ where the hardness was recorded as 280HV. The Gleeble results showed at peak temperatures the minimum hardness was 225HV.

Kim et al. [60] used laser tempering on fully hardened tensile boron steel coupons. They found laser tempering gave a uniform temperature distribution on the metal surface and that hardness measurements and tensile tests confirmed improved ductility in the heat affected area. In 3-point bend and axial crush tests the laser tempered press hardened steel showed no cracking.

Saha et al. [37] performed tests on a martensitic steel using different tempering modes using a Fiber Laser Welding (FLW) and Diode Laser Welding (DLW). Samples from the sub-critical HAZ were prepared for analysis. The growth kinetics of the precipitate carbides were suppressed when the samples were rapidly tempered using the FLW. The FLW samples showed more dispersed finer

carbides. Samples subjected to a DLW showed the highest recovery of dislocations due to greater heat input and higher tempering parameters. Overall rapid thermal cycles showed less ferrite grain recovery. Higher dislocation density was retained due to the shorter temper times. The strength of the dislocation density was found to be higher than that of the precipitation strengthening in tempered martensite. Rapidly tempered martensite was shown to have higher precipitation strength.

1.2.4.3 Induction and Resistance Tempering

Gleebles are often used for comparison or simulation of welding experiments. Gleebles can be used to precisely control experimental parameters such as temperature and time to accurately simulate welding procedures and to observe the effects of tempering. Heating in a Gleeble can be described as resistance heating. Induction heating is a process where electromagnetic induction is used to heat an electrically conductive material [61].

Ahn et al [62] found that cementite particles began to change from needle shape to spheroidal shape around 600°C with a tempering time of 40s in a Gleeble. With insufficient time, the matrix softening included dislocation annihilation and recovery, resulting in a slower rate of softening at high temperatures. When tempering at low temperatures, 300-500°C, the small inter-particle spacing of the rod-shaped cementite particles would hinder the movement of the mobile dislocations. This was observed after the material had undergone some strain. The yield strength was higher at lower tempering temperatures for the induction heated steel compared with conventionally tempered steel in this study.

In work done by Hedegard and Aslund [61], hot-formed martensitic boron steel was subjected to induction tempering before spot weld welding was investigated. The purpose of this work was to reduce local strain and cracking of HAZ after spot welding. Induction tempering was performed to

distribute strains and avoid localization around welds. High strain rate 3-point drop tower tests were performed on a full scale B-pillar with tempered flanges which showed promising results in improving energy absorption and reducing crack initiation.

A paper produced by Lee et. al [63] saw delayed carbide formation at higher temperatures and a nucleation of small carbides at 450°C for 15 s in a 0.45C steel. High frequency induction tempering was used to heat the samples at 50 and 70 °C/s for 15s hold times. The size of the carbides decreased and the spheroidization increased as the tempering temperature increased, and strong carbide forms Cr and Mo produced nano sized carbides. As the temperature increased so did the carbide forming elements. Induction heating reduced the tempering time for carbide spheroidization.

Biro et al. [58] used a Gleeble 3500 to better explore the relationship and characterise the rapid tempering process as it happens in a martensitic steel in DP steels. In the literature there is a variation from what is recorded experimentally and what is calculated for the JMAK values. The softening kinetics were derived from a series of rapid isothermal experiments designed to allow for the calculation of the tempering activation energy and rate exponent. It has also been found in other research that the JMAK model is unable to adequately model the low temperature softening data. It was postulated that the discrepancies were due to multiple processes occurring during tempering, it was tempering related to carbide nucleation and growth could be split into Stage I and Stage II softening. For the first stage of softening, the JMAK exponent n , agree with the literature for particle nucleation on dislocations. The carbide nucleation stage was found to occur very quickly, as tempering was experimentally observed and recorded for short tempering times and with tempering values less than 420°C. Martensite continues to decompose as tempering time increases. This is due to ferrite recrystallization, grain growth, and softening associated with carbide growth. It was found

that the process which dominates softening in Stage II is carbide coarsening. Stage II of softening was found to be inconsistent with literature values for the JMAK exponent and activation energy.

Sackl et. al [64]. Observed some small, spherical carbides suggesting cementite refinement at higher temperatures. Induction heat treatments were used on heat treatable 42CrMo4 steel. They observed for rapid (2 s) tempering heat treatments of up to 700°C limit dislocation recovery, thereby providing increased nucleation sites for the formation of fine, dispersed cementite particles. This reduction can provide increased nucleation sites for the formation of fine, dispersed cementite precipitates. Several very coarse irregular shaped carbides can also be observed within the microstructure of both samples.

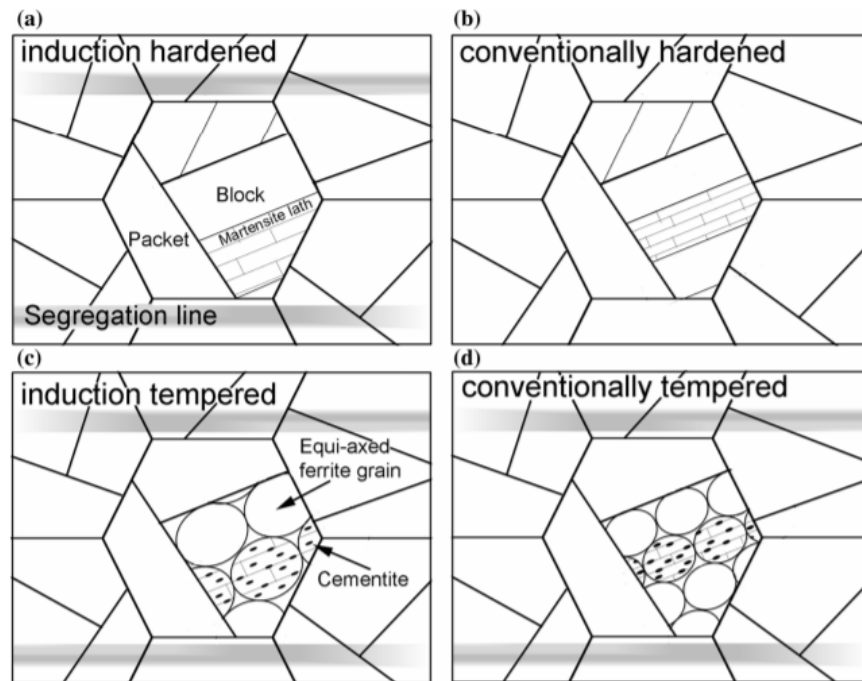


Figure 9: Schematic drawing of the microstructural evolution of heat treatable steel (a) after induction and (b) conventional hardening and (c) after induction and (d) conventional hardening and tempering. Adapted from [64]

Saha et al. [37] also subjected the tested material to induction heating in a Gleeble. The samples were heated at a rate of 100 °C/s to a temperature of 495 °C and held for 1s. The samples heated in a

Gleeble exhibited a comparatively less tempered structure when compared with the laser welded samples and had more finely distributed carbides. Elongated carbide precipitate shape was found in the Gleeble heat treated samples as well as less recovery and a higher amount of dislocation density retained. These samples also had more constant hardness values due to less softening of the boundary area, and higher precipitation strength contributions to overall strength.

Judge et. al [65] performed experiments to understand tempered martensite embrittlement during quenching and tempering. Short cycle tempering to overcome tempered martensite embrittlement was used and were performed in a Gleeble using press hardening steel received from ArcelorMittal. It was found that for cycle times from 300-400°C for 1 s, hardness measurements were more greatly varied than in the conventionally tempered counterparts of the same hardness. The toughness was enhanced using this method.

1.3 Research Intent

In this research two steels with higher carbon contents than are currently being used commercially were studied. The steels in this research have been designated as steel A, referring to the steel with lower carbon content, and steel B, referring to the steel with higher carbon content.

A series of experiments were performed on both steels and are outlined in the following section. These experiments have been designated as Part I and Part II. Both experiments involved subjecting blanks cut from sheets of both steels to two heat treatments in a Gleeble thermal mechanical simulator. Both experiments explored the affect of heat treatments on the resulting microstructures and hardness of the steels in question. The affect of the heat treatments on the two steels were compared for the same heating conditions.

1.3.1 Part I – Austenite Decomposition Model Optimization

The first series of experiments performed in this research involved imposing critical cooling rates on both

steels in the Gleeble thermal mechanical simulator. The resulting hardness of each quench condition was found and the area phase fraction for each condition was quantified. The cooling rates and chemical compositions of the steels were then imposed in the FE software LS-Dyna in the card *MAT_244. Using LS-Dyna the volume phase fractions of phases for each quench rate and steel were predicted. The predicted volume phase fractions were compared with the measured area phase fractions from the experiments. The predicted volume phase fractions from LS-Dyna were improved by comparing them to the values found for the quantified area phase fractions by adjusting the activation energy parameter of ferrite and bainite (Q_2 and Q_4). This experiment was performed on both steels and the predicted LS-Dyna values were improved for both steels.

1.3.2 Part II – Short Cycle Tempering

The second experiment performed on both steels involved imposing two heating cycles in the Gleeble thermal mechanical simulator on the steel blanks. The first cycle austenitized the blanks to create a fully martensitic microstructure. The heating profile was provided for the material by the industry partners. The second heating cycle involved imposing short cycle tempering heating profiles on the austenitized blanks. The tempering temperatures ranged from 100 to 700 °C and the tempering times ranges from 0.5 to 15 s. The resulting microstructures for both materials were characterized and the evolution of carbides was observed. The softening response for both materials was found through hardness measurements, and the resulting softening for both steels compared.

2. Experimental Methods

2.1 Materials and Equipment

Two steels with different carbon contents were studied in this work. Below is an explanation of the materials and equipment used to conduct the experiments in this work. The steel which contains a lower carbon content will be referred to as Steel A. The steel containing a higher carbon content will be referred to as Steel B.

2.1.1 High Carbon Ultra High Strength Press Hardening Steel

Both steels used in this research had a high carbon contents and are designated as Ultra High-Strength Steels (UHSS) post press hardening and were supplied by Ford. The nominal thickness of the sheets which blanks were made from for experimentation for Steel A was 1.7mm. The nominal thickness of the sheets were for steel B were 1.6mm. The chemistry of both steels can be seen in Table 1. The carbon content directly impacts the martensitic strength of the steel. Both steels have more carbon present than the conventional grade of 22MnB5 (0.22 %C) press hardening steel. The remainder of this section will include the equipment and methods used to prepare the specimens for the Gleeble Thermo-Mechanical Simulator (or Gleeble for brevity) experimentation and metallographic observation.

2.1.1.1 Steel composition

To determine the chemical composition of both materials, ICP (Inductively Coupled Plasma) analysis was conducted. This technique was used to determine the chemical composition of both steels used in this research. In this process, steel is first dissolved in acid and the vaporized with a plasma torch. The elemental composition of the material is then identified using atomic emission spectroscopy. The

samples were analyzed by Element Materials Technology in Cambridge Ontario. The analysis adhered to ASTM standards (D1976-18Mod and E1019-18). The ICP chemical analysis results can be seen in Table 1.

Table 1: ICP analysis performed by Element Materials Technology on Steel A and B

	Al	C	Cr	Cu	Mn	Mo	Nb	Ni	P	S	Si	Ti	V
Steel A	0.042	0.30	0.36	0.01	0.58	0.20	0.044	0.39	0.009	<0.005	0.56	0.020	<0.005
Steel B	0.033	0.32	0.31	<0.01	0.61	0.15	0.044	0.36	0.012	<0.005	0.57	0.021	<0.005

2.1.1.2 Gleeble Blank Geometry

The blank geometry for the purposes of the Gleeble experiment had to be designed in order to minimize the heat gradient along the length of the specimen. The length of the sample was made to be the maximize length that could fit in the Gleeble. The width of the sample for the purposes of the experiment were based on the dimensions found in [33]. The blanks were created from as-received steel sheets and cut with a mechanical shear. Two ¼ inch diameter holes were then drilled with a space of 157mm apart from each hole center. Both holes were drilled in the center of the blank. The center of the blanks as well as the areas surrounding the holes were sanded to remove the coating to improve contact between the blank, the thermocouples, and the gleeble grips.

2.1.1.3 Metallographic Preparation Materials

To prepare the heat-treated blanks for metallographic observation, they were first hot mounted in Struers conductive phenolic mounting resin. After this, the samples were polished to a mirror finish. The chemicals used to do this were Stuers DiaPro diamond suspension solutions. Three different suspension solutions were used. The suspensions used were 9 μm , 3 μm , and 1 μm , which correspond with the three polishing steps used in the sample preparation. Nital etchant was used after polishing had been completed to identify the composition of phases of the microstructure for each different heat treatment condition. A 3% nital solution was used to etch the hot mounted specimens for 2-20 second. The ASTM standards followed related to etchant nital are described in E407-07 Etchant #74s procedure for Iron based steels [66]. The application of nital allowed for the microstructure of the steels to be observed in a field emission scanning electron microscope (FE-SEM).

2.1.2 Equipment

2.1.2.1 Machinery

For the creation of the blanks a metal shear was used to cut pieces of the specified dimensions from the sheets of both steels. A milling machine was then used to drill holes on either side of the blank a specific distance from the center. A milling machine was used to achieve precise tolerances for experiment repeatability and heat gradient consistency.

2.1.2.2 Gleeble Thermo-Mechanical Simulator

A Gleeble 3500 was used in this research to heat treat the blanks. The Gleeble is able to precisely control the heating and cooling temperature-time profiles imposed on the specimens. For this research, a Gleeble was used to heat and cool the blanks very precisely for three different heating and

cooling cycles. These conditions, in conjunction with the Gleeble, were used to mimic heating and cooling cycles which may be seen in industrial application of press hardened steel. A quench head was also designed for the Gleeble to improve the repeatability and consistency of the experiment.

2.1.2.3 Dynamic Systems Inc. Thermocouple Welder

Thermocouples were welded to the center width and length of the samples for each experiment setup. To do this, a thermocouple spot welder was used. One wire was first clamped vertically in the welder, and the sample placed below. To prepare a sample, first the hood of the machine was covered and then the start button pushed. The thermocouples then dropped onto the samples and were welded in place.

2.1.2.4 FEI Quanta 250 Field Emission Scanning Electron Microscope

To obtain high-resolution micrographs of the microstructure of the material after heat treatment, a FEI Quanta 250 FE-SEM was used. Micrographs of up to 40000x magnification were obtained using the FE-SEM. These micrographs were then used to identify the phases present in the final microstructure as well as the carbide state. The phases identified in the micrographs were ferrite, bainite, and martensite.

2.1.2.5 Clemex MMT-M7 Micro-Hardness Tester

All hardness measurements were carried out using a Clemex MMT-M7 Micro-Hardness Tester. The load for each test conducted was 1000g. The hardness measurements from this machine are given Vicker's hardness.

2.1.2.6 Precision Saw

A Struers wet cut saw was used to cut the steel strips into small pieces without damage the surface through heat caused by friction. It also allowed for precise locations along the blank to be cut.

2.1.2.7 Struers Hot Mounter

A Struers hot mounting machine was used to hot mount each specimen to prepare it for metallographic analysis. The specimens were mounted in electrically conductive Polyfast resin to allow for observation in the FE-SEM as it is conductive.

2.1.2.8 Polishing System

A Struers LabPol-20 polisher holding a LaboForce 50 semi-automatic polishing head was used to grind and polish the surface of the specimens to a mirror finish. The speed and pressure of this polisher can be adjusted and it can polish up to four specimens at once.

2.1.2.9 Ultrasonic Bath

After each polishing step, an Ultrasonic Bath was used to clean each specimen. The specimens were submerged in 99% ethanol and cleaned in a minimum duration of 5 minutes in order to remove any diamond suspension particles which may contaminate the next polishing procedure. A Fischer Scientific M1800 1.9L Bath was used for this step.

2.2 Experimental Procedure

Below the procedure used to prepare and post process the samples is outlined. Please note that the Gleeble was used to conduct the experiments for Part I (Austenite Decomposition Model Optimization) and Part II (Short Cycle Tempering) of this work.

2.2.1 Gleeble Experimental Methodology

In these experiments the Gleeble was used to simulate the temperature-time profiles for Part I and Part II of this work. The Gleeble used for these experiments can be seen in Figure 12. The samples are heated using direct resistance heating, allowing for slow to very fast heating rates. Quenching is also very controlled through the application of back heating when over quenching is applied. For both experiments the blanks were first mounted in the mounting grips. Two different mounting grips designed for use in the Gleeble were applied for different situations in the experiments. For both experiments hot mount grips were used to heat the samples. Hot mount grips allow for reduced surface area contact between the blank and grips, allowing for a more uniform heating profile in the blanks. For the tempering experiment, copper grips were used. Copper grips allow for higher conductivity between the grips and blank. This allows for more precise heating. Both grips had small metal pegs which allowed for the blank to be secured by placing the metal pegs through the drilled holes in the blank on each grip.

Once the blanks were secured in the grips, the grips were placed in the Gleeble. The setting “run” was selected on the Gleeble interface and then the “mechanical setting” was selected. Using an adjustment tuner, the apparatus that holds the Gleeble grips was adjusted until the Gleeble grips were flush with the apparatus and a slight load to account for specimen buckling during heating could be applied. The load applied was 0.02kN and was adjusted by pulling the blank using the mechanical adjustment tuner. Once the blanks were secured with an applied load the thermocouples welded to the Gleeble were attached to the apparatus to record the blank temperature. After this the Gleeble door was closed

and the chosen program was run. This command was executed using a computer and the program Quiksim.

Quiksim was used to program the heating and quench parameters for the experiment. Quiksim was used to control the heating in temperature per minute increase. Each rate was coded as a different command in the program. A hold was represented as no rate change for the hold duration. Quenching was represented by turning the quench on. Quench 1 represents air while Quench 2 represents water. The cooling rate was input in the program, and the pressure the quench produced was adjusted using a pressure valve. The Gleeble applied backheating to adjust the temperature the thermal couples recorded. The current and therefore input heat is adjusted by the temperature recorded by the thermocouples.

In both simulations steel A and B were subject to the same heating profiles to compare the resulting hardness and microstructure in Part I and Part II of this work.

2.2.1.1 Part I - Constant Cooling Rate and In-Die Heating Simulation

In Part I of this work, both steel A and B were austenitized and the quenched within the Gleeble in order to determine the effect of cooling rate on phase transformations. The phase distribution of the Gleeble processed specimens is then quantified and the values are used to optimize a phase decomposition model. This section describe the Gleeble experiments only.

In these experiments, blanks were quenched at 5 different cooling rates. The Gleeble was used to heat, austenitize and quench the blanks. Based on the Gleeble experiments by Bardelcik et al. [33], the blanks were heated at a constant rate of 17 °C/s up to 600°C, then heated at 5 °C/s up to a temperature of 900°C. The temperature was then increased to a maximum of 977°C in 4 min and 20

s. It is important to note that this heating and austenitization profile applied to Usibor 1500, a grade of 22MnB5. Upon austenitization, four continuous cooling rates were imposed on four separate blanks made from Steel A and B. The continuous cooling rates used were 2.5, 5, 10 and 50 °C/s as shown in Figure 10. A non-isothermal quench condition was also imposed to simulate the thermal cycle of an in-die heating tailoring process. Two blanks were cooled at 18 °C/s and both held using a die temperature of 700°C. Two different hold times of 4 and 8 s were used to simulate the temperature during in-die heating. This temperature-time schedule was based on FE simulations of the in-die heating process as outlined in [67] and shown in Figure 11. The samples created using the 4 and 8 second hold will be referred to as ATM1, ATM2, BTM1 and BTM2 respectively. The nozzles of the quench head were oriented so that the spray was directed perpendicular to the length of the blank, producing a more even quench condition along where the thermal couples were positioned. A small tensile pre-load of approximately 0.3 kN was also applied to the blanks during heating in order to prevent buckling. The thermocouples were placed directly in the center of blanks for both steels and hot grips were used for all cooling conditions. The specimen was then removed for metallographic examination.

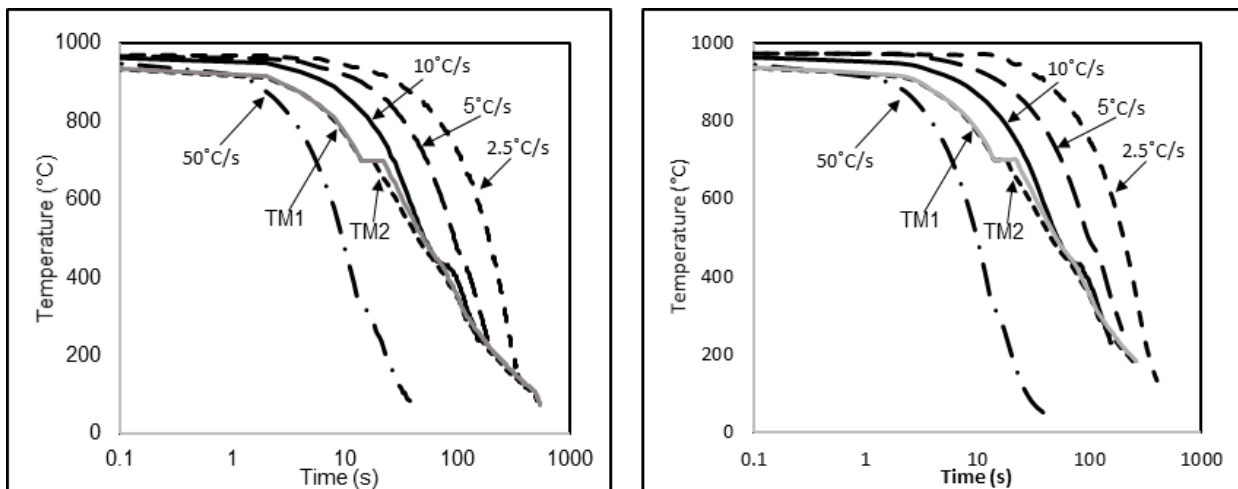


Figure 10: Quench Profiles acquired from the Gleeble for steel A (right) and steel B (left)

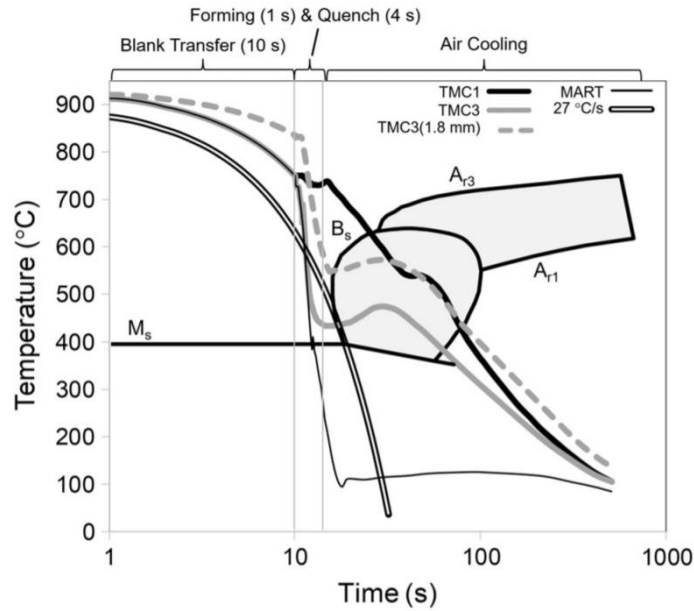


Figure 11: In-Die heating simulation curves, adapted from Bardelcik et al. [33]

2.2.1.2 Part II – Short Cycle Tempering Experiments

In Part II of this thesis, the Gleeble was used to investigate the effect of tempering temperature and time on fully quenched steel A and B specimens. Hardness tests and metallography was conducted on the Gleeble processed specimens.

Prior to conducting each tempering test, the Gleeble was used to process (create fully martensitic microstructures) the blanks using the press hardening temperature-time schedule according to the measured profile from a production line roller hearth furnace. This heat profile is intended for use on both steels for the purpose of producing press hardened parts which replicate the production process. For the press hardening and subsequent tempering simulations within the Gleeble, a small tensile pre-

load of 0.3 kN was applied to the blank in order to prevent buckling due to thermal expansion when the blank was heated. The heating rate was set to approximately 23 °C/s and the final temperature prior to quenching was above 900 °C. The blanks were heated for approximately 6 minutes. After this austenitizing treatment, the blank was quenched using water to room temperature to ensure a fully martensitic microstructure was produced. In industrial applications air quench would be preferred as water quench may produce finer microstructures. But for the purposes of producing a fully martensitic microstructure water quenching was deemed suitable. The quenched specimen was then removed from the Gleeble and the thermocouples were replaced with a new set of thermocouples. This was to reduce the chances of thermocouples becoming unattached during the short cycle tempering. The specimen was then placed back into the Gleeble for the tempering treatment. Micro-hardness testing and metallography was then conducted on the tempered specimen.

The tempering temperatures used in this study were; 100°C, 200°C, 300°C, 400°C, 500°C, 600°C, and 700 °C. The holding time at each temperature was also varies at approximately 0.5, 1, 2, 5, and 15 s. Once the tempering temperature was reached, the samples were held for the required time after which the blanks were water quenched to room temperature. Back heating was turned off during this process to reduce the chance of melting of samples near the grips. The measured temperature-time profiles for each tempering temperature can be seen in the appendices.



Figure 12: Gleble Thermal-Mechanical Simulator

2.2.2 Specimen Preparation

For both Part I and Part II, the Gleble processed blanks were cut with a precision wet saw into strips at the center of the blank where the thermocouple was located. The strips which were cut from the blank were then hot mounted with the cross sectional area of the center part of the strip facing down. The specimens were then plane ground starting with a Stuers 80 grit MD-Piano abrasive disc. Then

the specimens were each polished with 3 different polishing cloths and diamond suspension solutions. The first polished required 9 μm diamond suspension polish at 300 RPM polishing speed for 5 minutes with an applied force of 20 N. Next 3 μm diamond suspension solution was used at a polishing speed of 300 RPM for 5 minutes with an applied force of 20 N. The final polishing step included 1 μm diamond suspension solution at 300 RPM polishing speed for with a 10 N polishing force.

Before each polishing step, the specimens were cleaned with 99% ethanol in an ultrasonic bath. The specimens were placed in the ultrasonic bath for a maximum of 5 minutes to prevent contamination of suspension particles on successive polishing cloths.

After the specimens had been polished and cleaned they were etched using 1.5% nital solution. Etching was conducted in order to observe the steel microstructure. The samples were cleaned with 99% ethanol to prevent over etching.

2.2.3 Hardness Evaluation

All of the specimens created in both experiments were also prepared for micro-hardness analysis. The specimens were hot mounted and polished as described in the previous section. Micro-hardness measurements were taken with a Clemex MMT-M7 micro-hardness tester with a 1000 g load. Measurements with this instrument were taken on each mounted sample through-the-thickness of the specimen. The hardness of each indent was automatically measured using the Clemex software.

2.2.4 SEM Microstructure Evaluation

After the completion of specimen preparation and etching all samples were observed using a FE-SEM.

2.2.4.1 Part I - Phase Area Fraction Quantification

For Part I of this work, the Gleeble processed steels A and B were observed using the FE-SEM. High resolution micrographs were created for phase area fraction quantification. Three different images at a magnification of 4000x (549 x 394 μm) were used to quantify the area fraction of each phase for all the specimens. Image analysis software was then used to manually delineate the various phases in the SEM micrographs and quantify the area fractions as shown for example in Figure 13.

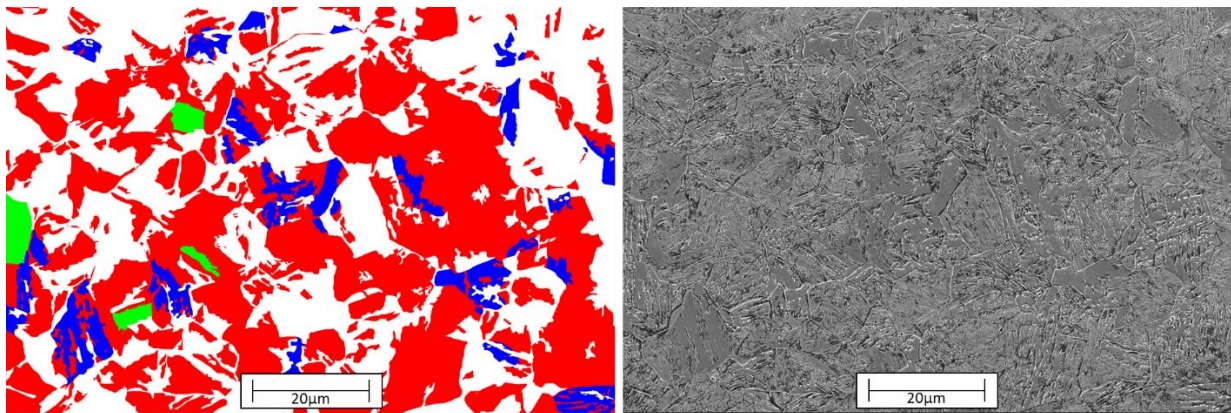


Figure 13: A post processed phase area quantification image with the original micrograph for comparison. The image pictured above is from TM2 for Steel A. The white is martensite (M), the red is bainite (B), the blue is ferrite (F), and the green is coarse bainite

2.2.4.2 Carbide Observation

For Part II of this work, the specimens tempered at 300-500-700 $^{\circ}\text{C}$ for 0.5, 1 and 15 s hold times were prepared for metallographic analysis. A specimen that did not undergo tempering was also prepared for examination. The FE-SEM was used to create high resolution micrographs. These

micrographs were taken at 20000x and 40000x magnification for observation of the tempered martensite microstructures.

2.2.5 LS-Dyna Simulation

For Part I, the cooling rates imposed in the Gleeble experiments were imposed on a single four noded shell element created in LS-Dyna to simulate the experiments. Both steel A and B were simulated and the predicted area phase decomposition was determined. The experimental cooling curves (Figure 10) were applied to the element as a thermal boundary condition. The measured chemistry in section 2.1.1.1 of both materials was used as input for the press hardening material model (*MAT_244) card and the remaining material model parameters were set to the default values as recommended by LS-Dyna. Upon completion of the simulations, the element history variable data was used to extract the predicted volume fractions and hardness for each cooling rate and steel chemical composition simulated.

2.2.5.1 Optimization Study

The results from LS-Dyna were manually optimized to produce similar results to the metallurgical observations. The activation energies of ferrite and bainite, Q_2 and Q_4 , were changed until the results began to converge. Convergence was based on the percent error between the simulated area fraction and observed area fraction for the three constant cooling rates 2.5°C/s , 5°C/s , and 10°C/s , reaching the minimum comparable value. The final optimized values of Q_2 and Q_4 were found for steel A and B. The activation energy for ferrite in LS-Dyna affects the resulting bainite area fraction, but the activation energy of bainite does not affect the final values of ferrite. The value of Q_4 was changed

until all percent errors began to approach a minimum comparable value. The effect of Q_2 was most pronounced on changes in ferrite area fraction with small changes in the activation energy.

3. Results and Discussion

This section will outline the results and provide discussion related to both parts of the research. First, Part I will cover the optimization of the austenite decomposition model us to simulate press hardening in LS-Dyna. Second, the effect of the short cycle tempering treatments (Part II) on hardness and microstructure for both steels will be presented and discussed.

3.1 Part I - Austenite Decomposition Model Optimization

3.1.1 Hardness Results

3.1.1.1 Steel A Critical Cooling Rate Hardness Results

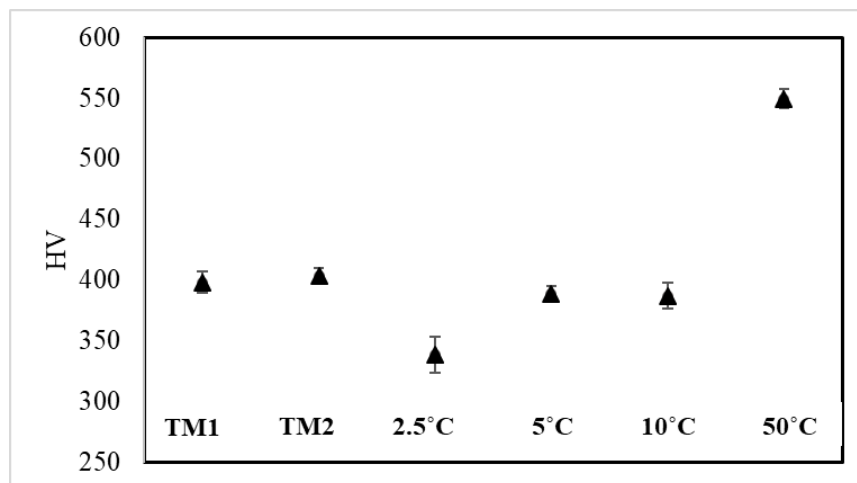


Figure 14: Critical cooling rate average hardness results and hardness standard deviation

Figure 14 shows the average Vickers hardness results taken from each sample. With the exception of the 2.5 °C/s and 10 °C/s specimen, the repeatability of the hardness measurements was more consistent. Upon conducting metallographic analysis, the measured scatter for the 2.5° C/s specimen was most likely due to localized regions of large grains within the multi-phase microstructure. This would result in individual tests indenting mainly a single phase rather than a mixed phase grain microstructure. Similar properties can be seen in the sample quenched at 10 °C/s as well as similar

variation in hardness measurements taken. Later metallography showed a microstructure mainly composed of lath martensite with areas of ferrite and bainite within the martensite. The sample quenched at 2.5 °C/s had an average hardness of 325 HV and a standard deviation of 14 HV. The sample quenched at 10 °C/s had an average hardness of 382 HV and a standard deviation of 11 HV. The repeatability of the hardness improved with quench increasing quench rate and resulted in an average hardness of 389 and 549 HV for the 5 and 50 °C/s tests, respectively. The average hardness of the TM1 and TM2 samples were found to be 403 and 407 HV, respectively.

Table 2: Steel A critical cooling rate hardness results

Quench Condition	Average Hardness
TM1	398
TM2	403
2.5 °C/s	339
5 °C/s	389
10 °C/s	382
50 °C/s	549

3.1.1.2 Steel B Critical Cooling Rate Hardness Results

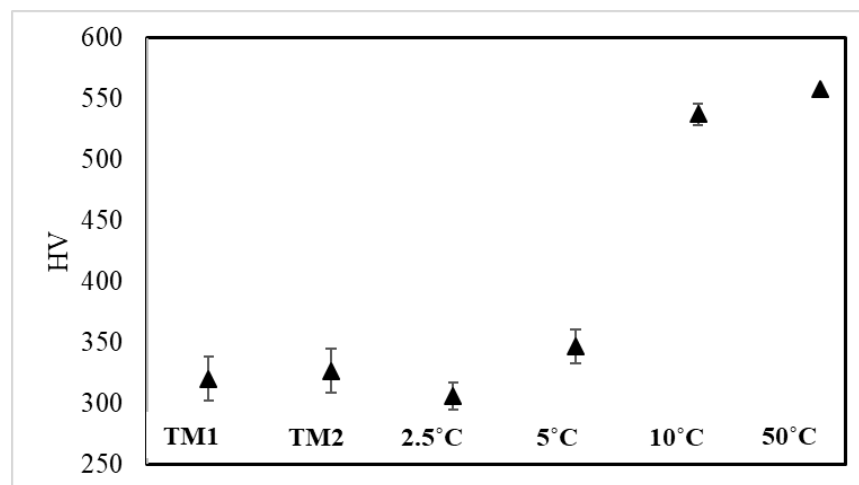


Figure 15: Critical cooling rate average hardness results and hardness standard deviation

In Figure 15 the average Vickers hardness results of the critically cooled specimens for Steel B can

be seen. The repeatability of the hardness measurements improves with the quench. The samples from TM1 and TM2 show the largest hardness variation compared with the other samples cooled below 50 °C/s from Steel B. The hardness for TM1 and TM2 are 320 and 326 HV respectively. Metallographic analysis of the microstructure in the FE-SEM revealed large areas of martensite and ferrite grains leading to varying hardness when indenting. A similar variation in hardness can be seen in the samples quenched and 2.5 and 5 °C/s, though not as large. The hardness of the sample quenched at 2.5 °C/s had an average hardness of 306 HV and a variation of 11 HV. The hardness of the sample quenched at 5 °C/s has an average hardness of 347 and a variation of 14 HV. The hardness of the sample quenched at 10 °C/s has an average hardness of 537 HV and a variation of 9 HV. The hardness of the sample quenched at 50 °C/s has an average hardness of 559 HV and a variation of 4 HV. The variation of the TM1 and TM2 samples are both 18 HV.

Table 3: Steel B critical cooling rate average hardness results

Quench Condition	Average Hardness (HV)
TM1	320
TM2	326
2.5 °C/s	306
5 °C/s	347
10 °C/s	537
50 °C/s	559

3.1.1.3 Steel A and B hardness results comparison

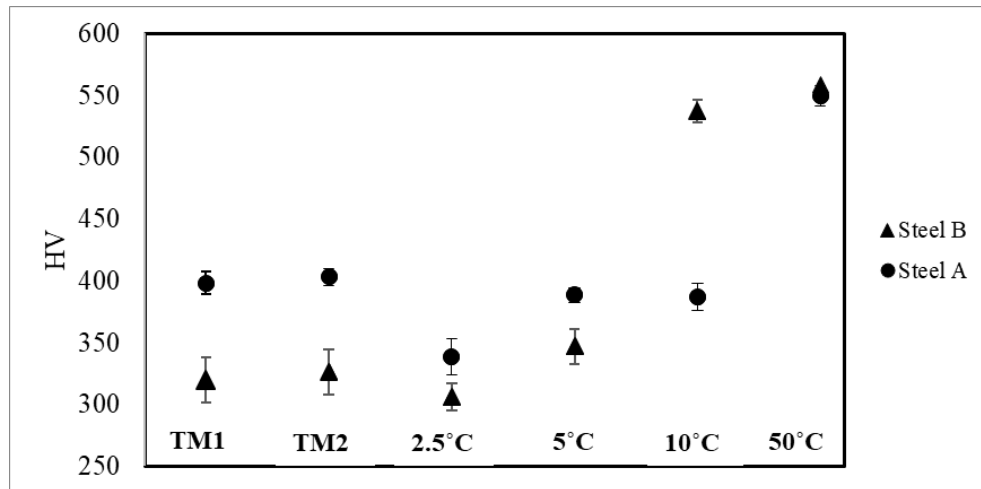


Figure 16: Average hardness results for Steel A and B – I would also include error bars for these?
Why is your x-axis missing?

A comparison of the average hardness results can be seen for Steel A and B in Figure 16. The average hardness of Steel A is greater than that of Steel B for TM1, TM2, 2.5, and 5 °C/s. The hardness of Steel B at the quench rate of 10 and 50 °C/s is greater than that of Steel A. The percent carbon in Steel B is higher than in Steel A which leads to greater hardness as the quench rate increases. Due to the chemistry of Steel A, at the lower quench rates the steel maintains a higher hardness. Results from observations under an FE-SEM show at the lower quench rates large grains of bainite within the microstructures of Steel A. In Steel B, the dominant phase found was ferrite, which would be the main factor contributing to the difference in hardness of both steels at low quench rates. The difference in variation between both materials also reveals the difference between phases expressed in the microstructure. The samples from Steel A were dominated mainly by bainite, leading to more repeatable hardness measurements. In contrast, Steel B had more equal areas of each phase constituent. This would affect the variance in Steel B and increase the inconsistency of hardness values recorded. Steel B softens more than Steel A, which would make it more attractive for use in tailoring operations.

3.1.2 Microstructure Results

3.1.2.1 Steel A Microstructure Results

The average percent area phase can be seen in Table 4. The values in this table represent the average area phase fraction found through the manual post processing of 3 images of each sample of 4000x magnification. These results represent the percent of each phase found for each quench condition.

Table 4: Critical cooling rate microstructure average area phase results for Steel A. Represented in () is sample error.

	2.5 °C/s	5 °C/s	10 °C/s	50 °C/s	TM1	TM2
Bainite	70 (5)	67 (5)	67 (7)	-	59 (7)	45 (7)
Martensite	17 (2)	29 (7)	32 (8)	100	37 (8)	51 (7)
Ferrite	13 (4)	4 (2)	1 (1)	-	4 (2)	4 (1)

The microstructure of the 2.5 °C/s test consists of bainite (70%), ferrite (13%), and martensite (17%) as shown in Figure 17a. and c. and quantified in Table 4. In the resulting microstructure for this cooling rate no pearlite was observed. The ferrite observed is a flat and featureless constituent, while the martensite grains form at grain boundaries (and junctions) and have lath-like characteristics. Bainite appears in the microstructure of this quench condition as both coarse and fine carbides within the ferrite matrix. The fine carbides observed in this microstructure can be described as upper bainite (B). Upper bainite appears as fine carbides oriented along a common direction and dispersed throughout the bainitic ferrite matrix. The coarse bainite observed in this microstructure is similar to that of a granular bainite (GB) phase, which is characterized by either martensite or retained austenite (M/A) within a ferrite matrix [33]. The carbides appear as large rectangular shaped islands of martensite oriented along a common direction within the ferrite matrix.

The microstructure of the sample quenched at 5 °C/s consists of a refined grain distribution of bainite

(67%), ferrite (4%) and martensite (29%) as shown in Figure 17. Compared to the 2.5 °C/s test, the bainite area fraction is nearly unchanged, while the ferrite content is reduced and the martensite content increases. The increase in martensite content resulted in the increase in measured hardness for this specimen. The majority of the bainite observed is that of an upper bainite (B) type, while the amount of GB has decreased, as has the size of the GB grains.

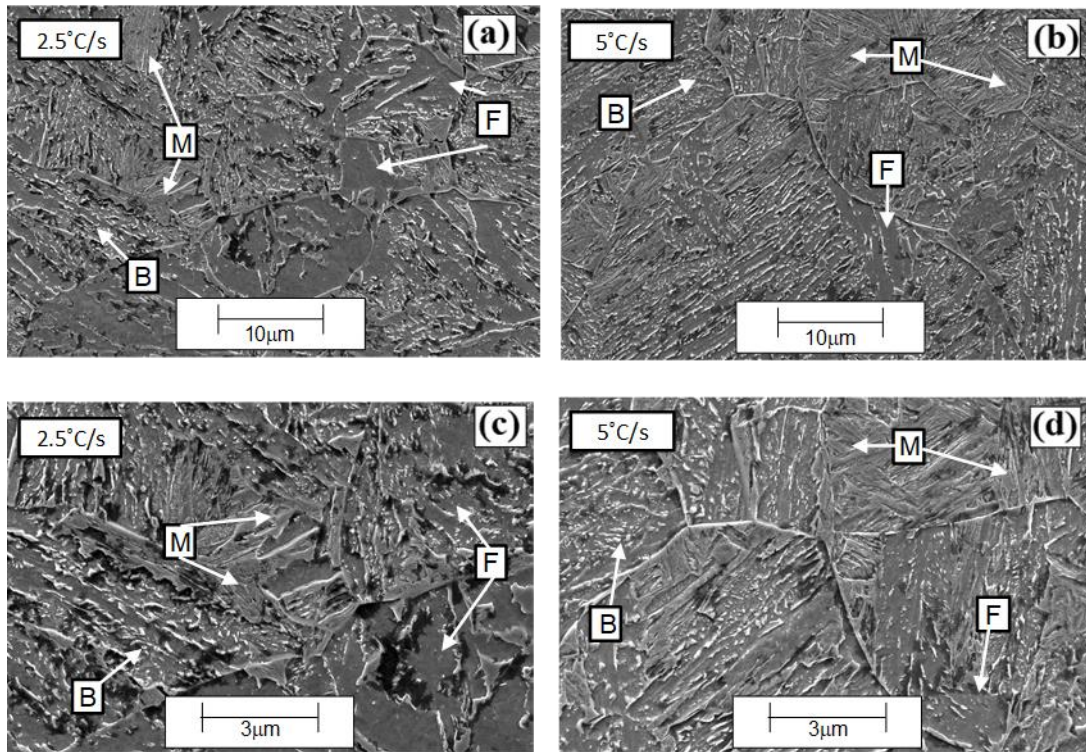


Figure 17: SEM micrographs for resulting quench conditions of 2.5 °C/s and 5 °C/s for Steel A

The microstructure of the sample quenched at 10 °C/s consists of bainite (67%), ferrite (1%) and martensite (32%) as shown in Figure 18 a. and c. This microstructure is similar to the microstructure observed for the 5 °C/s specimens and can be confirmed by the similar hardness of both. The martensite and bainite grains appear to have formed at the prior austenite grain boundaries, which resulted in a large and uniformly distributed grain structure. There was very little GB observed. The microstructure of the 50 °C/s test was martensitic as shown in Figure 18 b. and d. This aligns

with the high measured average hardness of 549 HV. The martensite appears as mostly lath-like with a few grains consisting of finely distributed carbides. These carbide rich regions may be evidence of auto-tempered martensite within the microstructure. In work conducted by Jarvinen et al. [51], the effect of the paint baking treatment of 170 °C for 20 mins on 30MnB5 and 34MnB5 was shown to produce tempered martensite. The tempering process resulted in the formation of fine iron carbides within martensite laths that appear similar to those observed in Figure 18d.

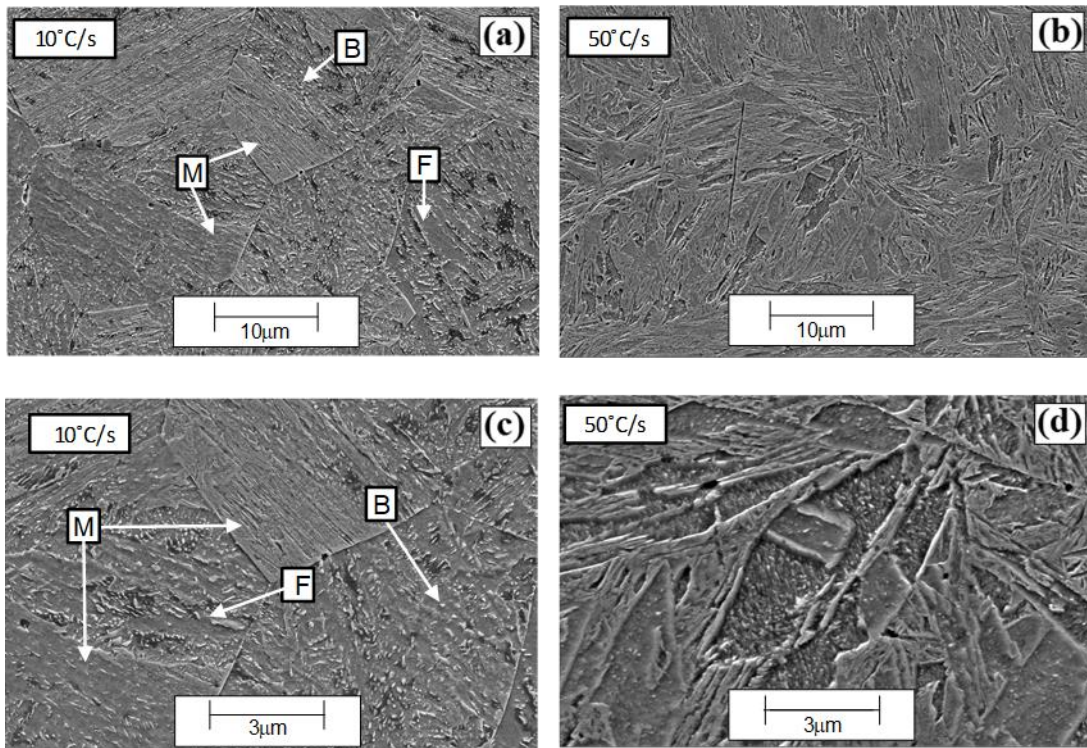


Figure 18: SEM micrographs for resulting quench conditions of 10 °C/s and 50 °C/s for Steel A

The microstructure of TM1, seen in Figure 19 a. and c., is composed of martensite (51%), bainite (45%) and a small amount of ferrite (4%). TM2, seen in Figure 19 b. and d., consisted of martensite (37%), bainite (59%) and a small amount of ferrite (4%). Some GB was observed for both material conditions, with the TM2 GB microstructure consisting of a more coarse structure than TM1. It

should be reiterated that the only difference between these two quench conditions is that the TM1 specimens were held at 700°C for 8 s, while the TM2 specimens were held for 4 s at the same temperature. Because the Continuous Cooling Transformation (CCT) diagram is unavailable for this material, it can only be assumed that the longer holding time for TM1 resulted in more bainite transformation as the temperature-time curve entered the bainite window of the CCT diagram. The longer holding time may have also resulted in more tempering of the GB for TM2, which may have resulted in the observed coarsening for this material when compared to TM1. Although not quantified, it is apparent that the overall microstructure of TM2 is more refined than TM1 as shown Figure 19. Also, the measured hardness of TM1 and TM2 is similar, even though TM1 consists of 14% more martensite than TM2. Therefore, the grain refinement of the TM2 materials may have elevated the strength (or hardness) to match that of TM1.

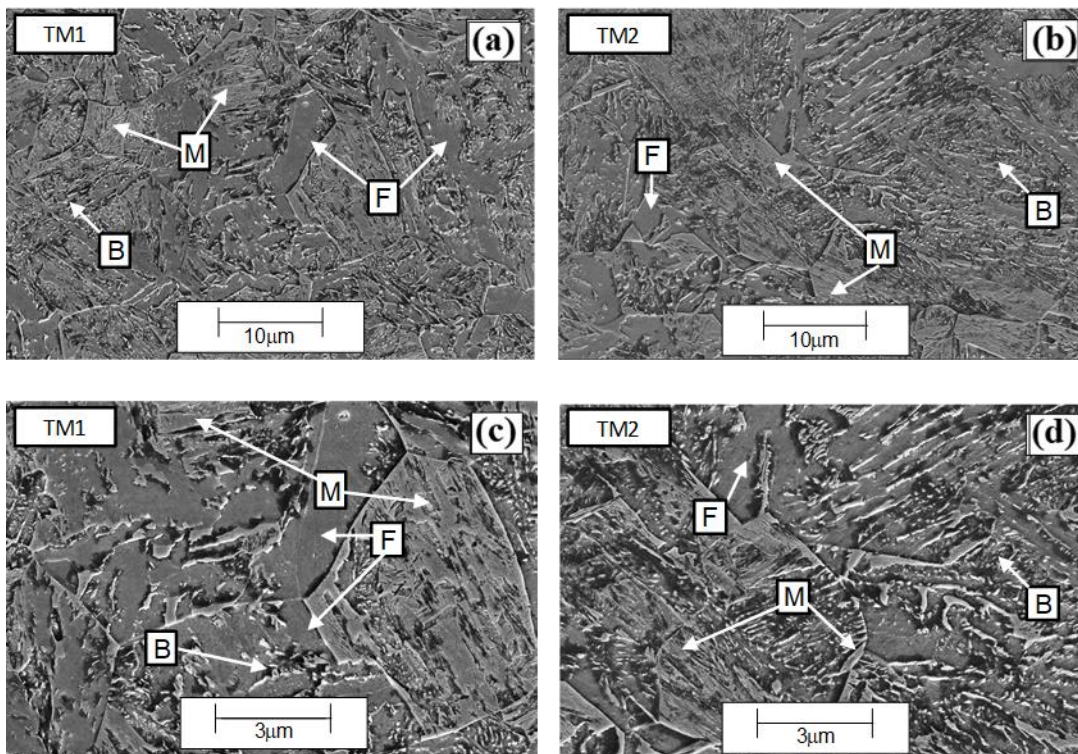


Figure 19: SEM micrographs for resulting quench conditions of TM1 and TM2 for Steel A

3.1.2.2 Steel B Microstructure Results

Table 5: Critical cooling rate microstructure average area phase results for Steel B. Represented in () is sample error.

	2.5 °C/s	5 °C/s	10 °C/s	50 °C/s	TM1	TM2
Bainite	20 (4)	33 (5)	3 (2)	-	25 (6)	40 (8)
Martensite	36 (15)	39 (16)	93 (1)	100	38 (4)	37 (5)
Ferrite	44 (12)	28 (16)	4 (1)	-	37 (3)	23 (5)

The microstructure of the sample quenched at 2.5 °C/s consists of ferrite (44%), bainite (20%), and martensite (36%). Micrographs of this quench condition can be seen in Figure 20 a. and c. Large grains of ferrite (F) can be seen in this microstructure, appearing both within and around martensite grains. The martensite (M) appears lath-like and can be seen throughout the microstructure at grain boundaries and junctions. There is also bainite (B) visible in this microstructure, appearing as carbides within the ferrite matrix. Very course carbides appear at a greater frequency within this microstructure compared to the microstructures of the same quench rate Steel A. The bainite observed in this microstructure can be described as upper bainite. Upper bainite is characterized by finely dispersed plate-like carbides found inside a ferritic matrix. This could mainly be due to the change in phase area of fraction between both steels at this quench rate with, with Steel A being a mainly bainitic microstructure. Very course carbides can be seen within the resulting microstructure for a quench rate of 2.5 °C/s which may be described as granular bainite and lower bainite. This bainite is characterized as martensite or retained austenite islands within a ferritic matrix oriented along the same axis as stated before. The bainite mainly seen within the microstructure of this quench rate could be described as upper bainite, with some instances of granular bainite being observed.

The resulting microstructure of the sample quenched at 5 °C/s consisted of bainite (33%), ferrite (28%), and martensite (39%). The micrographs can be seen in Figure 20 b. and d. The microstructure of the quench rate 5 °C/s shows larger phases of microstructural constituents than the quench 2.5 °C/s. Compared with the quench rate of 2.5 °C/s, the microstructure of the sample quenched at 5 °C/s is more coarse. In this sample, the area phase fraction of bainite has increased while the area phase fraction of ferrite has decreased. The area phase fraction of martensite has marginally increased. There is an increase in granular bainite visible within this matrix, but the bainite of this microstructure continues to be mainly composed of upper bainite. The decrease in ferrite and increase in bainite result in an increased measured hardness for this quench rate.

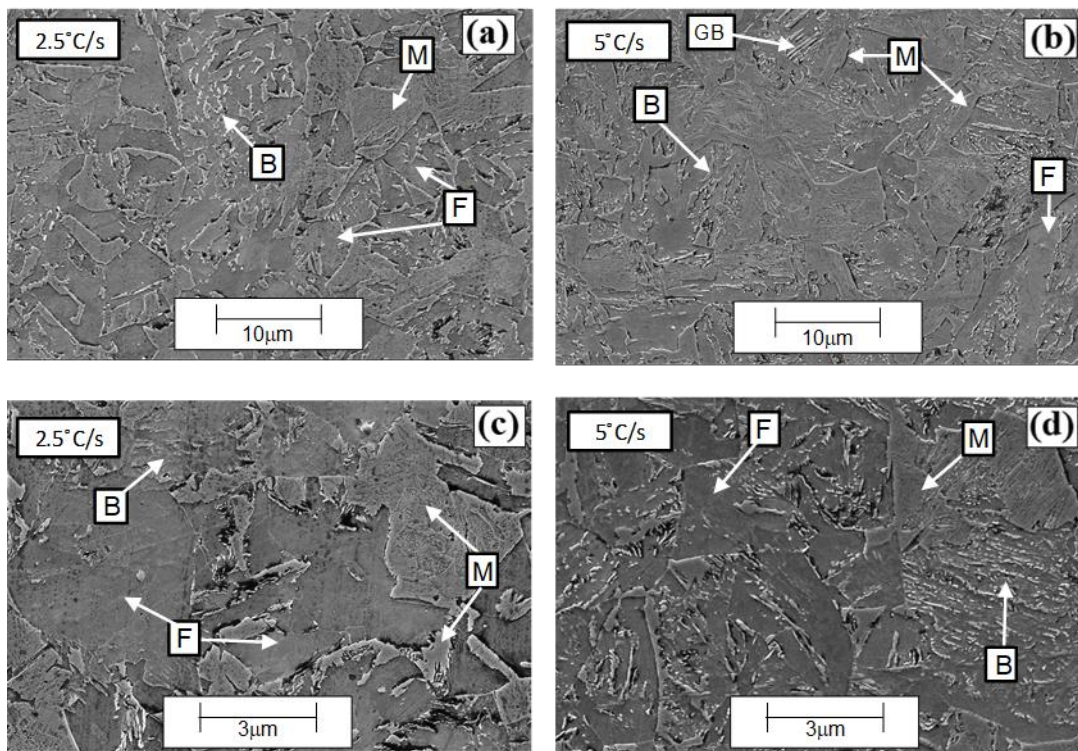


Figure 20: SEM micrographs for resulting quench conditions of 2.5 °C/s and 5 °C/s for Steel B

The microstructure of the sample quenched at 10 °C/s consists of bainite (3%), martensite (93%), and ferrite (4%). This can be seen in Figure 21 a. and c. The resulting microstructure from this quench

conditions is almost entirely martensitic. The martensite observed is lath martensite with small grains of ferrite and bainite between laths. There are also a few small areas of very fine carbides between laths, which may be indicative of auto-tempering. The resulting hardness of this quench condition is much greater than for the quench rates of 2.5 °C/s and 5 °C/s. The increase in martensite at this quench rate compared with the same quench rate for Steel A is mainly based on the increased carbon content in Steel B. The martensite appears to have formed at prior austenite grain boundaries and there is no granular bainite observed.

The resulting microstructure of the specimen quenched at 50 °C/s for Steel B can be seen in Figure 21 b. and d. This is to be expected given quench rate. The hardness values from this specimen also support this finding, being around 559 HV. The microstructure is primarily lath martensite with some very small spherical carbides scattered through the lath. There are several very small grains of fine carbides within the lath martensite as well and appear spherical in shape. The appearances of these very fine grains of carbides may indicate auto-tempering occurring in the Gleeble. When compared with the sample cooled at the same cooling rate for Steel A, the phases of carbides in between the martensite grains are smaller in area and the quality of the carbides are finer.

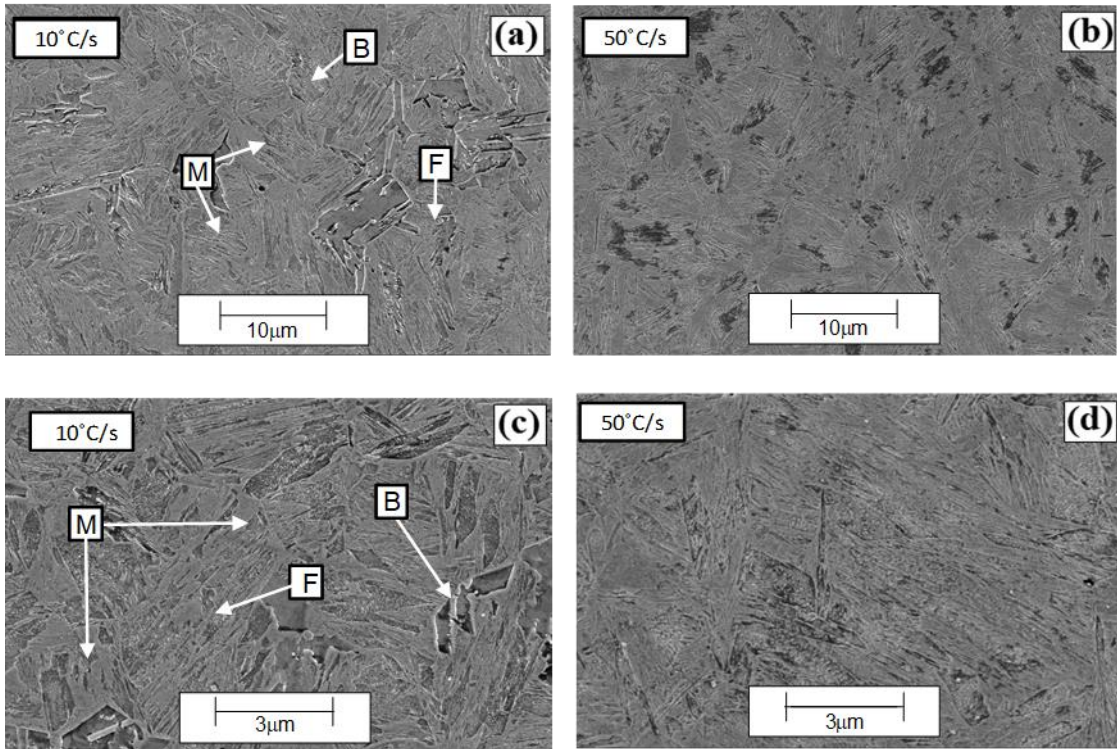


Figure 21: SEM micrographs for resulting quench conditions of 10 °C/s and 50 °C/s for Steel B

The microstructures of TM1 and TM2 for Steel B are composed of martensite, bainite and ferrite. The microstructure of TM1 consists of bainite (25%), martensite (38%), and ferrite (37%). The microstructure of TM2 consists of bainite (40%), martensite (37%), and ferrite (23%). In both resulting microstructures GB could be observed. More GB was observed in TM2 than TM1. There was no observable difference between the coarseness of the microstructures, but TM2 retains more bainite compared to TM1. It can be assumed for Steel B that a longer holding time results in a microstructure with less bainite and more ferrite. For both conditions the area phase fraction of martensite remained nearly constant. The amount of martensite appears greater in TM1 but a small amount and in the micrographs quantified it is clear some area of the microstructure contains larger areas of martensite than others, but overall it may have less martensite. There is more GB observed in TM2 than TM1, but this may be due to tempering of coarse carbides and martensite islands into

ferrite. The measured hardness for both conditions are similar, being 320 and 326 HV for TM1 and TM2 respectively. The change in hardness is likely caused by increased bainite and decreased ferrite in TM2 compared to TM1. Both TM1 and TM2 appear to have a similar coarseness as the microstructures quenched at 2.5 °C/s and are less coarse than the microstructures from the sample quenched at 5 °C/s. TM1, TM2 and the quench rate of 5 °C/s have similar percent area phases, but different hardness. As the quench rate of 5 °C/s produced a more coarse microstructure, it is likely that areas being indented were primarily martensitic. TM1 and TM2 both have more refined microstructures, there for a greater mix of phases possibly being indented during hardness testing.

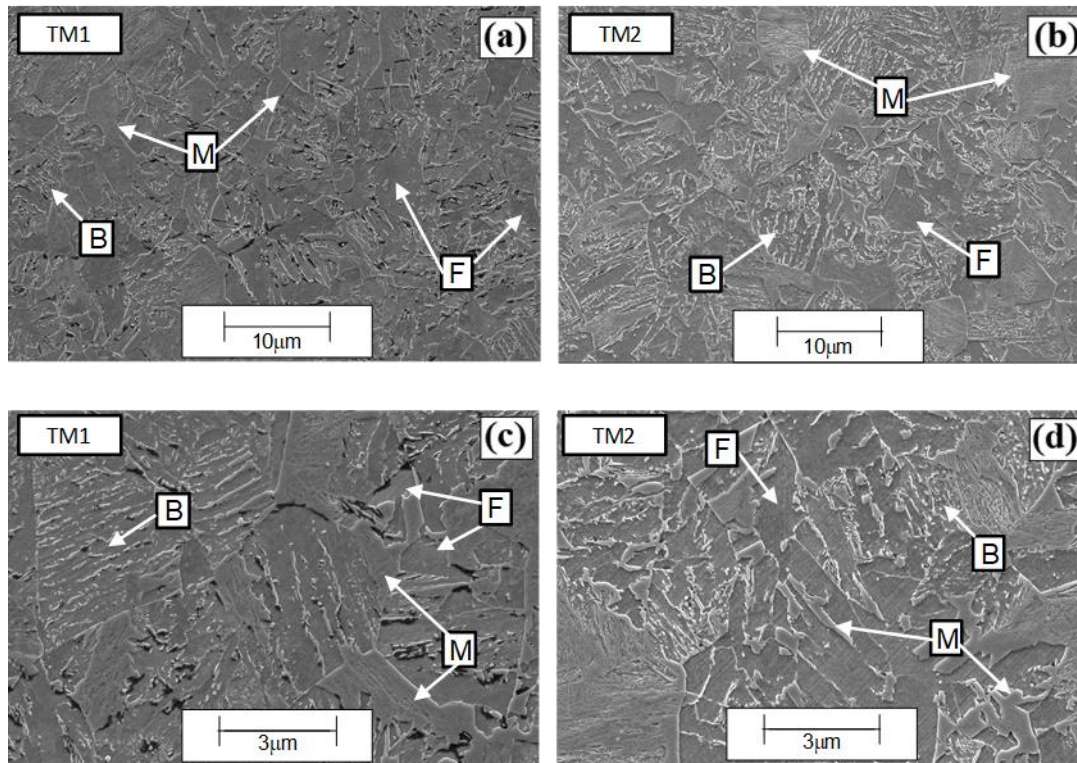


Figure 22: SEM micrographs for resulting quench conditions of TM1 and TM2 for Steel B

3.1.3 LS-Dyna Simulation Results

3.1.3.1 Steel A Simulation Results

The volume fractions of the as-quenched phases for Steel A were predicted through the LS-Dyna FE

simulations and the results can be seen in Table 6. Please note that these simulation used the suggested default model parameters in the LS-Dyna user manual. The most accurately predicted volume phase fraction by the simulation was from the quench rate of 50°C/s . A fully martensitic transformation was predicted by the simulation which was found from observation and hardness testing in the sample. For the other constant cooling rates were not able to predict the correct as-quenched microstructures with much accuracy. For the $2.5 - 10^{\circ}\text{C/s}$ tests, the model tended to over predict the ferrite phase fraction transformed and under predicted the martensite and bainite phase fraction. The activation energy values used in LS-Dyna for ferrite (Q_2) and bainite (Q_4) from austenite were optimized for use with 22MnB5 grades of press hardening steel. This could mean the default activation energy values for simulations using higher carbon steels may not simulate correctly the phase decomposition. Omer et al. [27] have shown that an appropriate calibration of the activation energy parameters can lead to better predictions of sub-critical phase transformation for 22MnB5. Using this methodology the activation energies where optimized for this steel and the results are presented in section 4.1.4.1. Another model parameter which may have contributed to the poor predictions is the austenite grain size which was not measured in this work. The austenite grain size is a component of the Kirkaldy rate equation used to predict the decomposition of austenite. For the TM1 and TM2 quench conditions, the models over predicted the bainite and ferrite content and under predicted the martensite content. The transformation predictions for predicted hardness and phase volume fraction for all of the cooling rate (except 50°C/s) specimens were inaccurate. The predicted (using default LS-Dyna model parameters) volume phase fraction results can be seen in Table 6. The results for the average hardness, the predicted hardness with default Q_R parameters, and the predicted hardness with optimized Q_R parameters are presented in

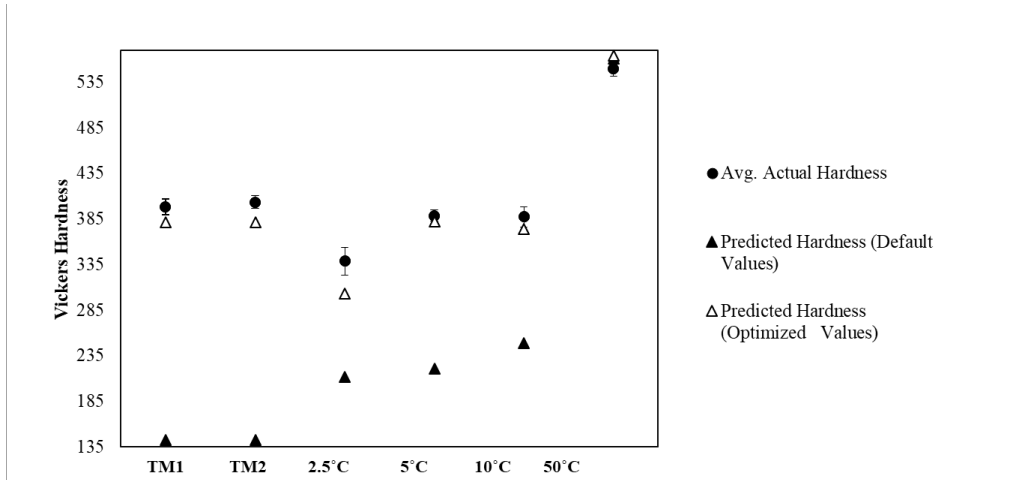


Figure 23 for Steel A.

Table 6: The Measured (M) and Predicted (P) as-quenched microstructure constituents for Steel A

	2.5 °C/s		5 °C/s		10 °C/s		50 °C/s		TM1		TM2	
	P	M	P	M	P	M	P	M	P	M	P	M
Bainite	23	70	21	67	39	67	-	-	75	59	77	45
Martensite	1	17	3	29	4	32	99	100	13	37	13	51
Ferrite	76	13	76	4	57	1	1	-	12	4	10	4

3.1.3.2 Steel B Simulation Results

The results for the volume fraction of the as-quenched phases produced by the LS-Dyna were extracted from the results of the FE simulation and the values from the default parameters can be seen in Table 7. The simulation accurately predicted the resulting microstructure for the quench rate of 50 °C/s, similar to the simulation with Steel A. All other as-quenched microstructures were not accurately predicted. The simulation, as a possible result of being tuned to accurately predict the phase decomposition of Usibor1500, over predicts ferrite for the volume phase fraction results for higher carbon steels. Like before, martensite and bainite continue to be under predicted, but for the case of this steel, the underprediction of martensite is significant. For the quench conditions of TM1

and TM2, the model continues to over predict bainite and under predicts ferrite. Steel B, more than Steel A, has relatively balanced area phase fractions, and the simulation results have proven to favor one phase over the others due to the bias of the activation energies. The hardness predicted by LS-Dyna are also in poor agreement with the measured hardness. The results for the default LS-Dyna hardness of each quench condition can be found in Figure 24 and Table 7. The austenite grain size was also not measured in this study and therefore not used a parameters to tune *MAT_244 for this steel to improve the as-quenched microstructures predicted by LS-Dyna. The optimized results and activation energies can be seen for Steel B in section 4.1.4.2. The average hardness, the predicted hardness with default Q_R parameters, and the predicted hardness with optimized Q_R parameters are presented in Figure 24 for Steel B.

Table 7: The Measured (M) and Predicted (P) as-quenched microstructure constituents for Steel B

	2.5 °C/s		5 °C/s		10 °C/s		50 °C/s		TM1		TM2	
	P	M	P	M	P	M	P	M	P	M	P	M
Bainite	25	20	34	33	4	3	-	-	75	25	75	40
Martensite	4	36	5	39	85	93	99	100	22	38	23	37
Ferrite	72	44	61	28	11	4	1	-	3	37	2	23

3.1.4 LS-Dyna Optimization

3.1.4.1 Steel A Optimization Results

Table 8: The Measured (M) and Optimized Predictions (O) as-quenched microstructure constituents for Steel A

	2.5 °C/s		5 °C/s		10 °C/s		50 °C/s		TM1		TM2	
	O	M	O	M	O	M	O	M	O	M	O	M
Bainite	67	70	63	67	72	67	1	-	60	59	60	45

Martensite	14	17	35	29	27	32	99	100	40	37	40	51
Ferrite	18	13	2	4	1	1	-	-	-	4	-	4

A simple optimization study was conducted to optimize the *MAT_244 activation energy values of ferrite (Q_2) and bainite (Q_4). This optimization was only based on the constant cooling rates of 2.5, 5, and 10 °C/s. Convergence was based on the percent error between the predicted volume fractions and measured area fraction. The default values of Q_2 and Q_4 were 10324 and 15068 J/mol, respectively. The optimized values of Q_2 and Q_4 were found to be 12174 and 15314 J/mol, respectively. In this optimization study, Q_2 was first modified until convergence had been achieved. The convergence was achieved when the percent areas between the measured and simulated phases became as close as possible in value. The elevated activation energy for ferrite slowed the ferrite transformation. This was then able to reduce the predicted ferrite and increased the predicted amount of bainite. The increase in bainite activation energy (Q_4) had a smaller effect on predicting the ferrite transformation. The final percent error between the observed and the simulated area fraction of bainite were between 3% and 9%. The final Vickers hardness from the simulation were 303, 382 and 374 HV for 2.5, 5 and 10°C/s, respectively. Due to the improved prediction of phase transformation for the optimized simulations, the resultant prediction of hardness also improved as shown in Figure 24. The optimized activation energies were also applied to the simulation for the cooling rate of 50°C/s, TM1, and TM2. The Vickers Hardness values for TM1 and TM2 (381 HV, 381 HV) improved but the predicted phase distribution of TM1 over predicts the bainite content and under predicted martensite content.

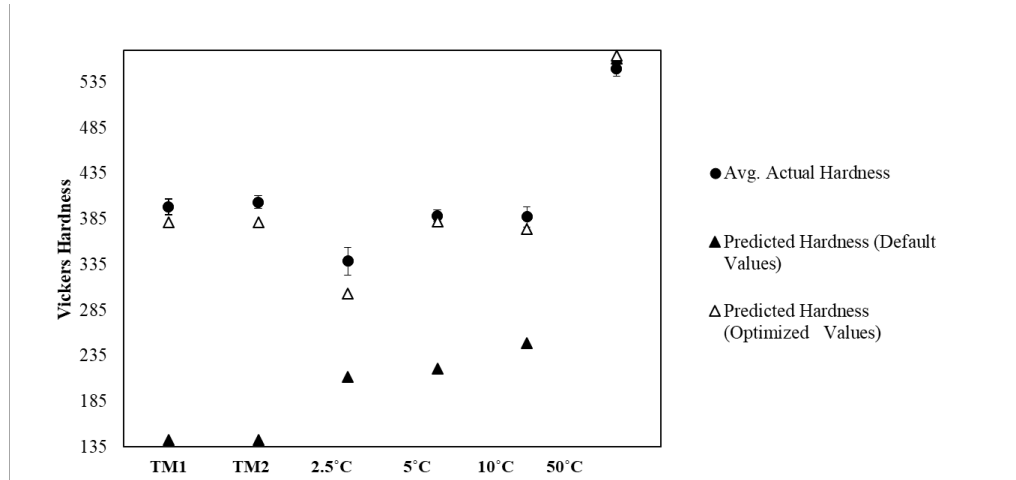


Figure 23: The average measured and predicted hardness for each quench rate for Steel A

3.1.4.2 Steel B Optimization Results

Table 9: The Measured (M) and Optimized Predictions (O) as-quenched microstructure constituents for Steel B

	2.5 °C/s		5 °C/s		10 °C/s		50 °C/s		TM1		TM2	
	O	M	O	M	O	M	O	M	O	M	O	M
Bainite	13	20	26	33	1	3	1	-	16	25	16	40
Martensite	21	36	57	39	97	93	99	100	83	38	82	37
Ferrite	66	44	17	28	2	4	-	-	1	37	2	23

A simple optimization study was conducted to optimize the *MAT_244 activation energy values of ferrite (Q_2) and bainite (Q_4). This optimization was only based on the constant cooling rates of 2.5, 5, and 10 °C/s. The methodology for convergence deviated from the previous optimization study on Steel A. The simulated volume phase fractions were not able to converge in a similar manner to the previous study, and the percent error between the cooling rate for each phase of bainite and martensite remained distinct. The difficulty in achieving convergence was similar as described in section 2.2.5.1 and may be due to the increase in bainite between the quench rate of 2.5 and 5 °C/s.

Therefore, the methodology to achieve the most accurate activation energies to replicate the measured phase fractions became based on when convergence of the standard deviation between the percent error for bainite and martensite. The bainite activation energy (Q_4) was chosen when the standard deviation for bainite and martensite converged. The default values of Q_2 and Q_4 were 10324 and 15068 J/mol, respectively. Using the method stated above the optimized values of Q_2 and Q_4 were found to be 10914 and 15538 J/mol respectively. The final percent error between the observed and the simulated area fraction of ferrite were 52%, 52%, and 47% for 2.5, 5, and 10 °C/s respectively. The final percent error between the observed and simulated bainite were 37%, 33%, and 76%. The final percent error for martensite was found to be 44%, 44%, and 4%. The elevated activation energy for ferrite slowed the ferrite transformation. The elevated activation energy for bainite slowed the bainite transformation. The activation energy for ferrite was found to be less in the optimization study for Steel B than in the optimization study for Steel A. The activation energy for bainite was found to be more in the optimization study for Steel B than in the optimization study for Steel A. The optimized values for the activation energies improved the hardness results for 2.5, 10, and 50 °C/s the most. The hardness results for these quench conditions are 274, 547, and 571 HV respectively. The hardness values for 5 °C/s, TM1 and TM2 were improved slightly by the optimized activation energies. The hardness results for these quench conditions are 420, 403, and 403 HV respectively. The simulated hardness now over predicts the hardness for these particular quench conditions. These three quench conditions have the most balanced phase area fractions, which holds them in contrast to the other three quench conditions which mainly produce one phase over the others. Due to these distinct difference between the area phase fraction of 2.5, 5, and 10 °C/s, satisfying optimization values could not be produced with the converged Q_2 and Q_4 values.

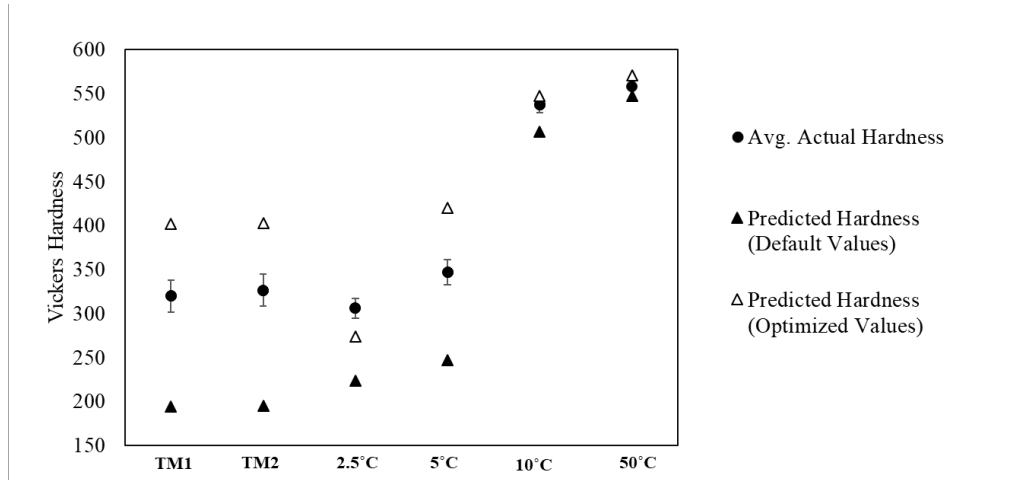


Figure 24: The average measured and predicted hardness for each quench rate for Steel B

3.2 Part II - Short Cycle Tempering

3.2.1 Hardness Results

3.2.1.1 Steel A

The effect of increasing tempering temperature shows a significant reduction in hardness for all the samples tempered from 0.5 to 15 s for Steel A. The heating and cooling tempering profiles for Steel A can be seen in Figure 26. The hardness results gathered from each sample can be seen in Figure 25. At the tempering temperature of 300 °C, hardness of all specimens begins to decrease. In general for all samples held from between 100 to 300 °C, the hardness remains unchanged at approximately 548 HV within an average deviation of 7 HV. The 15 and 5 s hold times result in a softer microstructure overall, but the hardness is maintained from 100 to 200 °C. The hardness also appears to peak for the sample tempered for 15 s for 300 °C and the sample held for 5 s at 200 °C. The maximum hardness occurs in the sample tempered for 15 s at 100 °C. The hardness of the specimens tempered for 1 s

increase compared to the other conditions at 400 and 500 °C. This may be the result of the precipitation hardening in the matrix. Precipitation hardening can slightly increase hardness at lower tempering temperatures as recrystallization cannot occur [36]. The higher hardness observed around 300 °C for the samples tempered for 0.5, 1, and 2 s may be due to high heating rates and its effect on when carbides precipitate compared with conventionally tempered samples at the same temperature [34]. There is a difference in hardness between the samples tempered at 300 °C for 0.5 and 15 s. The resulting microstructures can be seen in section 3.2.2.1. A possible cause for this result of the increase in hardness for the sample tempered at 300 °C for 1 s is an increase in microstructure refinement compared with the sample held for 15 s. The standard deviation is also slightly larger for the lower tempering temperatures than for the higher ones, which may be due to martensite tempering, coarsening of the carbides, or nucleation of carbides changing the hardness of the material throughout the sample. In a paper by Judge et. al [65] it was found that for cycle times from 300-400 °C for 1 s hardness measurements were more greatly varied than in the conventionally tempered counterparts of the same hardness.

The general trend of martensite softening as tempering temperatures increase is likely due to the recovery and recrystallization of martensite which begins to transform into equi-axed ferritic grains as carbides precipitate out of the metastable martensitic microstructure [35]. It appears that the rate of precipitate transformation between the shorter (0.5, 1 s) and longer (5, 15 s) hold times at the elevated tempering temperatures is not as significant due to the previously observed drop in average hardness of 20 HV for the 15 s specimens. The softening effect due to an increased tempering temperature has a more significant effect on hardness. In the paper by Gunnardottir and Basurto [59], the softening of the microstructures in that study produced similar trends for comparable tempering temperatures. The decrease in the magnitude of hardness as tempering temperature increases behaves similarly to what

was observed in the tempering of Steel A for 0.5 s.

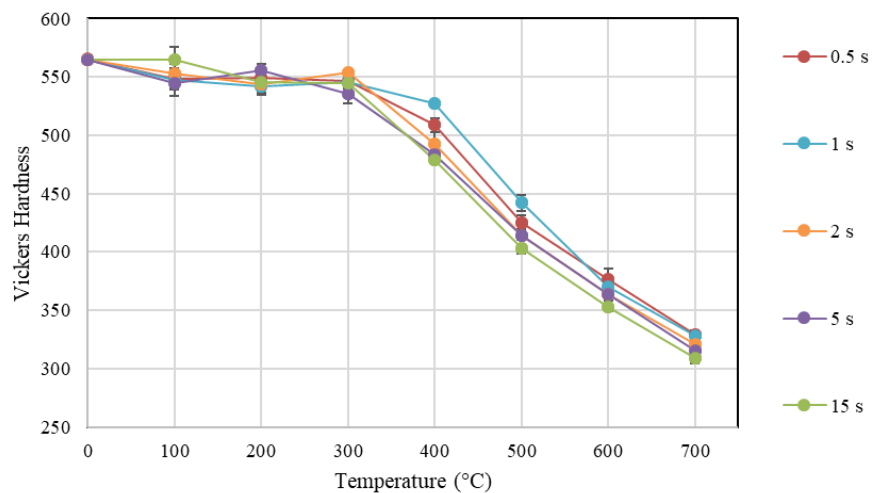


Figure 25: The resulting average hardness measurements for all tempering conditions and both hold times for Steel A

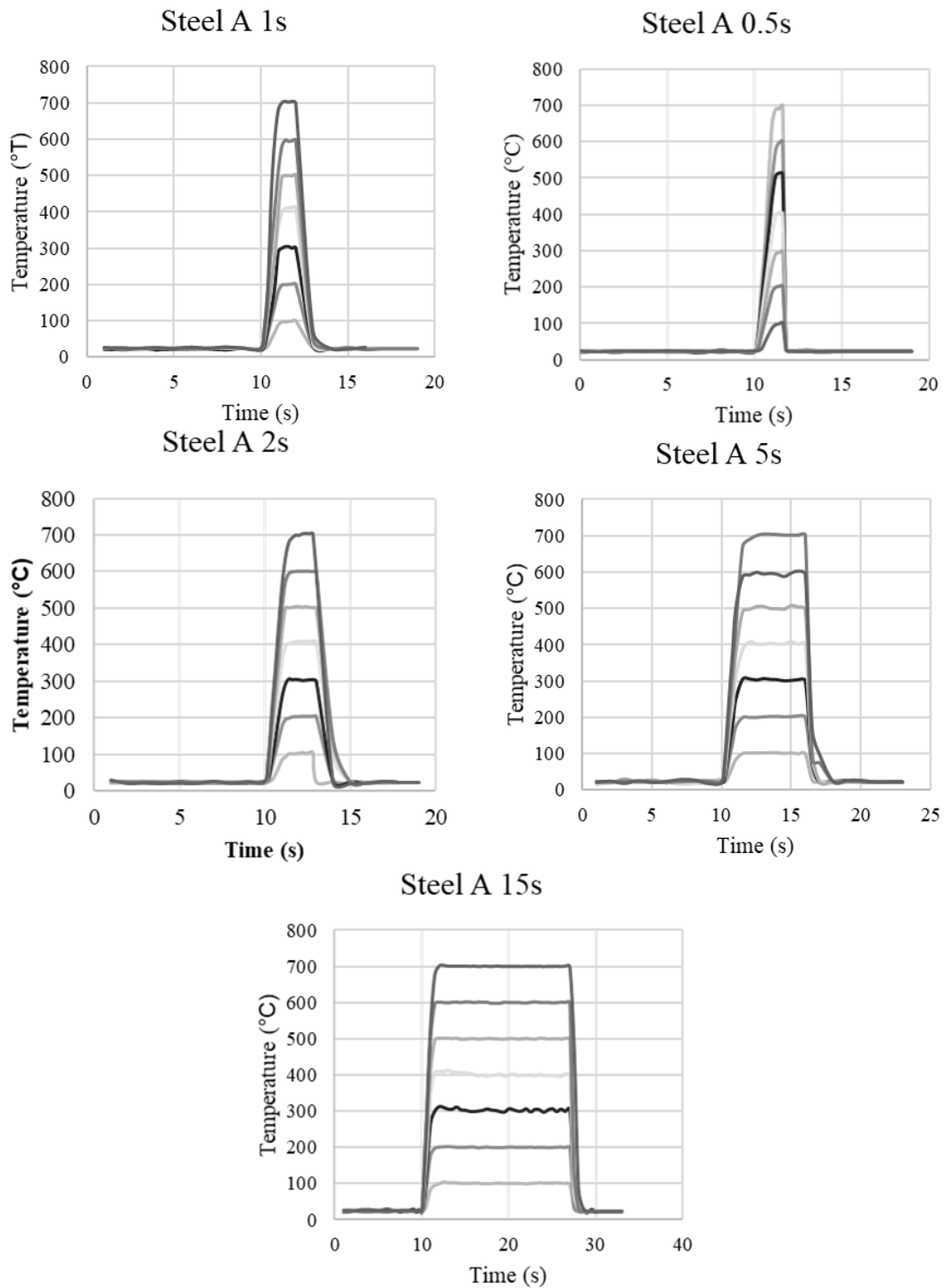


Figure 26: Heating and quenching profiles of the tempering cycle performed on Steel A for all temperatures and times fraction of heat up time to temperature is much longer for smaller times this may also be influencing your results

3.2.1.2 Steel B

The effect of increasing tempering temperature shows a significant reduction in hardness for all the samples tempered from 0.5 to 15 s for Steel B. The heating and cooling tempering profiles for Steel A can be seen in Figure 28. The average hardness measurements from each tempering condition can be seen in Figure 27. Similar to Steel A, at 300 °C the hardness for each sample begins to decrease. For tempering times of 100 °C, a major difference between the hardness of Steel A and B can be seen in the samples tempered at each time; the hardness for all the tempering times increase, with the exception of 15 s. The hardness of the sample tempered for 1 s at this temperature increases in hardness the most. This particular sample has an average hardness of 650 HV. This hardness is 45 HV above the hardness of the sample which had no post quenching heat treatment. These results may reveal a steel like Steel B may increase in hardness during a paint baking cycle. The hardening of microstructure of this steel after tempering at low temperatures for short cycles may be a result of precipitation hardening. The hardness for all samples begins to decrease after 300 °C after an initial hardening. The hardness decreases at a similar rate to that of Steel A. A convergence of the hardness of Steel A and B begins to happen between 300 and 400 °C. The hardness of the samples tempered for 1 s maintain a higher average hardness compared with the other tempering conditions. In the same tempering hold for Steel A, a similar trend of this tempering condition producing on average harder samples can also be seen. Similar to Steel A, the standard deviation is slightly larger for the samples tempered at lower temperatures than higher ones. This once again may be due to the nucleation and coarsening of carbides throughout the matrix, creating areas where there are large hardness differences. The extent to which Steel B softens compared to Steel A at higher temperatures and longer holds is greater. This is indicative that Steel B is more sensitive to temperature during

tempering than Steel A due to the extremes in hardness that can be seen.

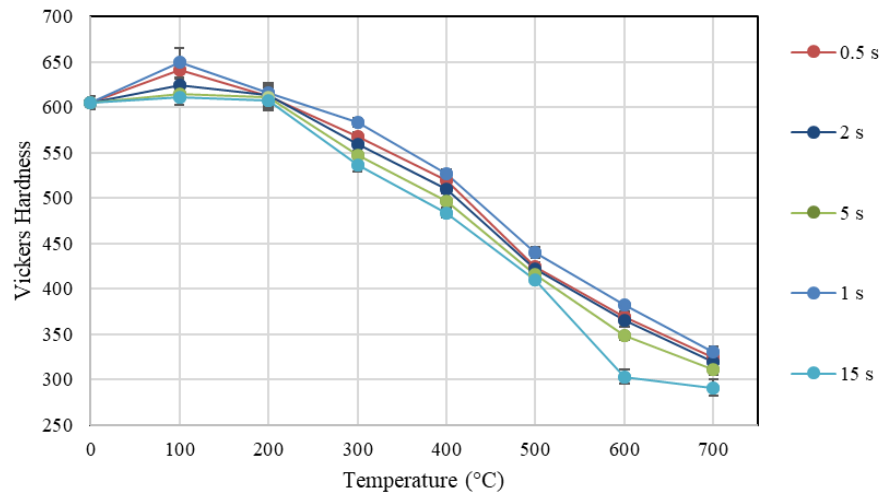


Figure 27: The resulting average hardness measurements for all tempering conditions and both hold times for Steel B error bars needs for hardness measurements as well as units on legend

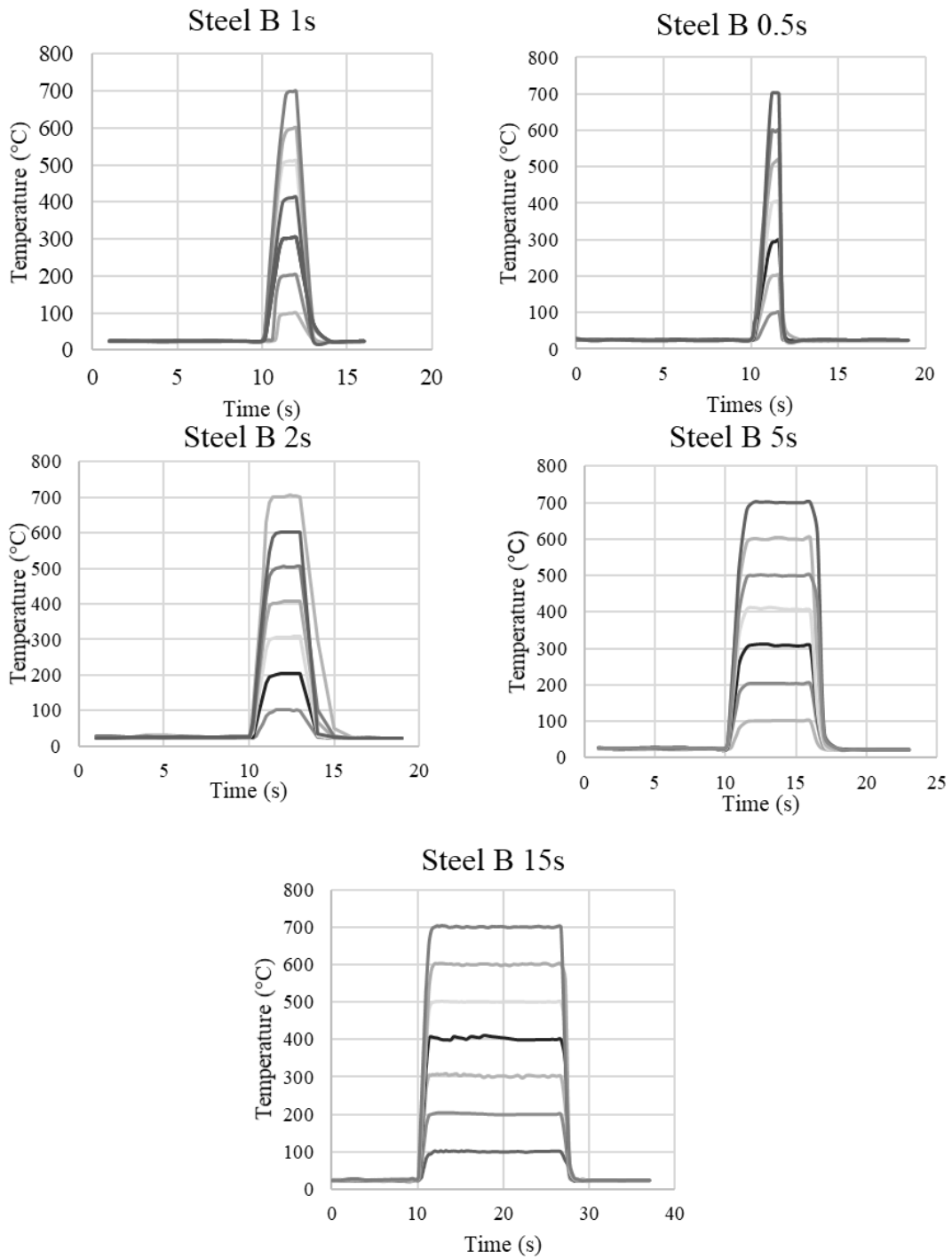


Figure 28: Heating and quenching profiles of the tempering cycle performed on Steel A for all temperatures and times

Comparisons of the hardness of Steel A and B for the same tempering hold can be seen in Figure 29. The changes in hardness for Steel A and B can be clearly seen in Figure 29 a. where the peak temperature of Steel B at 100 °C is almost 100 HV greater than Steel A. Steel A has an average change per hardness measurement of 56 HV and Steel B has a average change per hardness measurement of 60 HV after 300 °C. The softening of Steel B is much greater than steel at 700 °C. This can be seen in Figure 29 e., where the final hardness measurement for Steel B is 15 HV less than for Steel A.

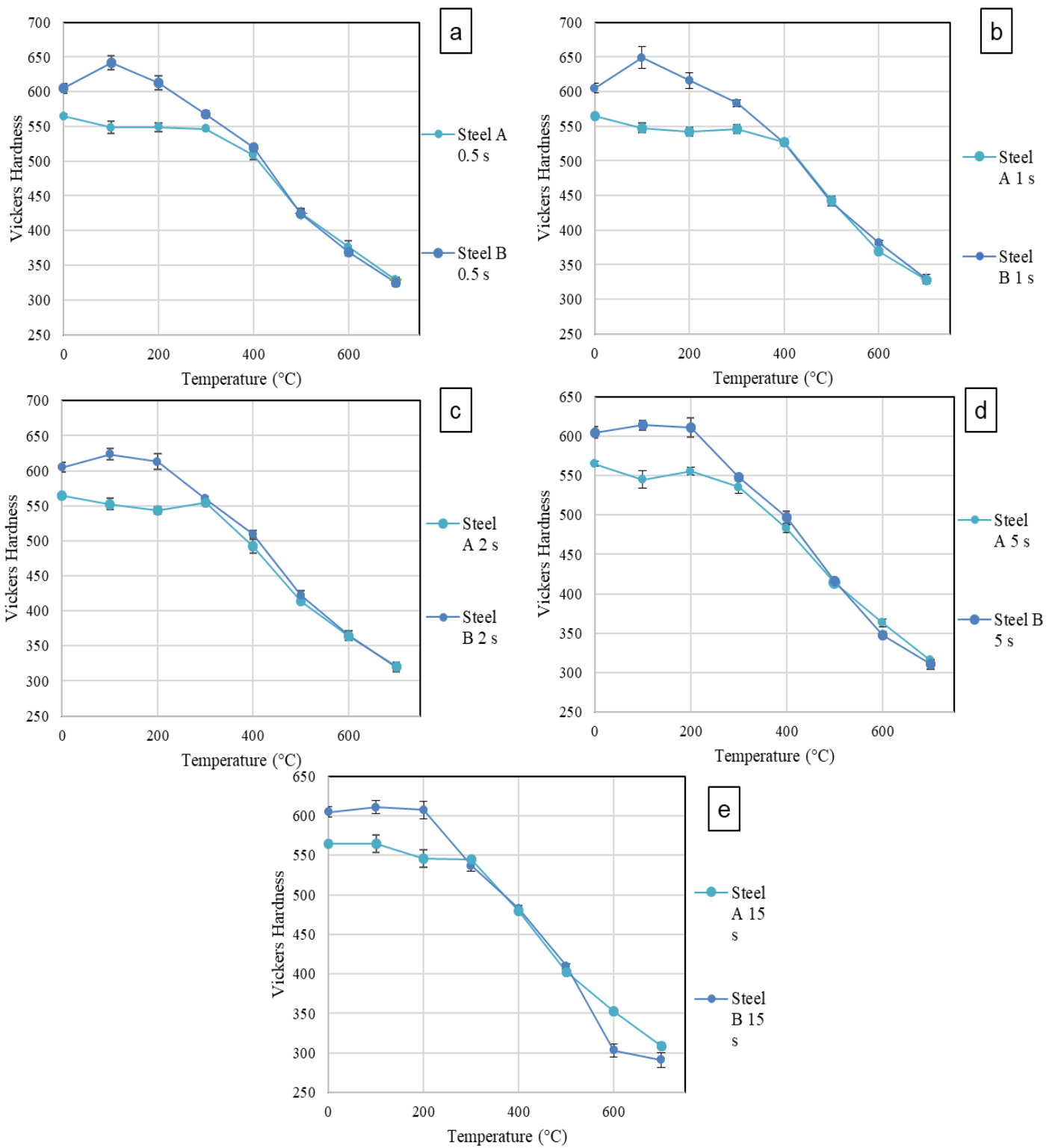


Figure 29: Average measured hardness for Steel A and Steel B. The figures a-e represent resulting hold times for both steels for the tempering times 0.5-15 s error bars needed for all graphs

3.2.2 Microstructural Analysis

3.2.2.1 Steel A Microstructural Results

Below are the resulting microstructures for the samples of Steel A tempered at 300, 500, and 700 °C and one fully hardened sample. The tempering times chosen were 0.5s and 15s. The different tempering times and temperatures create a variety of resulting conditions in the final microstructures as shown for the 300-500-700°C tempering conditions for both 0.5 and 15 s in Figure 31-Figure 33.

In Figure 30 micrograph of the fully hardened microstructure for Steel A can be seen. Each specimen before tempering began with the microstructure of Figure 30.

At a tempering temperature of 300°C the observed resulting microstructure is almost entirely martensitic for both tempering times. For a tempering time of 0.5 s the visible martensite has fine concentrated carbides within martensite grains and at prior austenite grain boundaries. The martensite observed is mainly lath martensite and it doesn't appear that many carbides have precipitated. This is confirmed by almost no change in hardness from the untempered sample. In contrast to the samples tempered at 300°C, the fully austenitized without heat treatment samples showed few fine carbides. Mainly small amounts of very coarse, spherical carbides can be seen in the microstructure. When held for 15 s at 300°C, the micrographs show a number of large, coarse carbides that precipitate as shown in Figure 31 b. These observations suggest that carbides are in the beginning stages of nucleation at a tempering time of 0.5 s. Tempering for 15 s results in softening due to carbide coarsening [68]. These observations occur at a small scale for this tempering temperature.

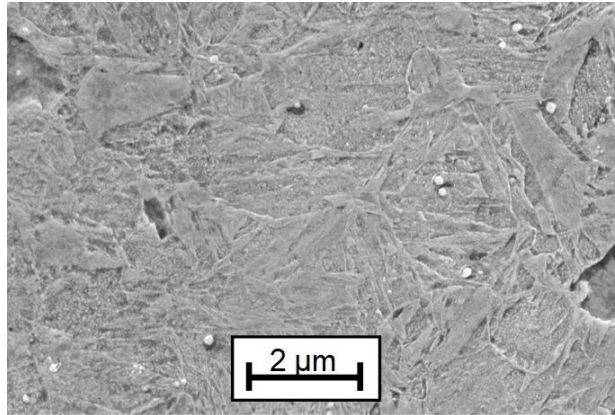


Figure 30: Fully quenched microstructure for Steel A

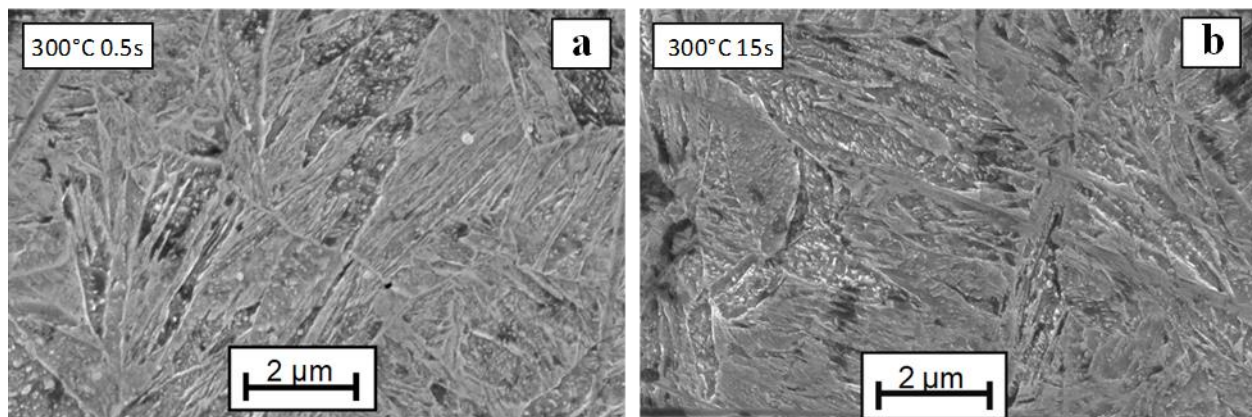


Figure 31: SEM micrographs of sample tempered at 300 °C for Steel A

The specimens tempered at 500 °C both contain clearly precipitated carbides as shown in Figure 32 a. and Figure 32 b. The carbides coarsen and then begin to appear ubiquitously throughout the microstructures. In general, the 0.5 s tempered specimens have more finely dispersed carbides than the 15 s specimens. The carbides also appear coarser for the sample tempered for 0.5 s and the density of carbides within the microstructure is lower. More carbides appear within the lath martensite structure for the material tempered for 0.5 s than for the material tempered for 15 s. For both tempering times, it is likely that precipitate nucleation is complete. It is also likely that martensite has begun precipitating into ferrite and cementite. This stage is referred to usually as Stage 4 in carbon steel tempering. Areas of ferrite can be seen for both tempering times. The small

difference in hardness could be due to a large amount of carbides visible within the microstructure of the sample tempered for 0.5 s. Less martensite also appears to have tempered in the samples held for 0.5 s. In a paper by Lee et. al [63], a delayed carbide formation at higher temperatures and a nucleation of small carbides at 450°C was observed for 15 s in a 0.45C steel. The implication here is that nucleation of carbides is not as far along for the sample tempered for 0.5 s than for the sample tempered for 15 s. Improved mechanical properties, such as the ones seen by Judge et. al [65] may occur for the shorter tempering times over a longer tempering period.

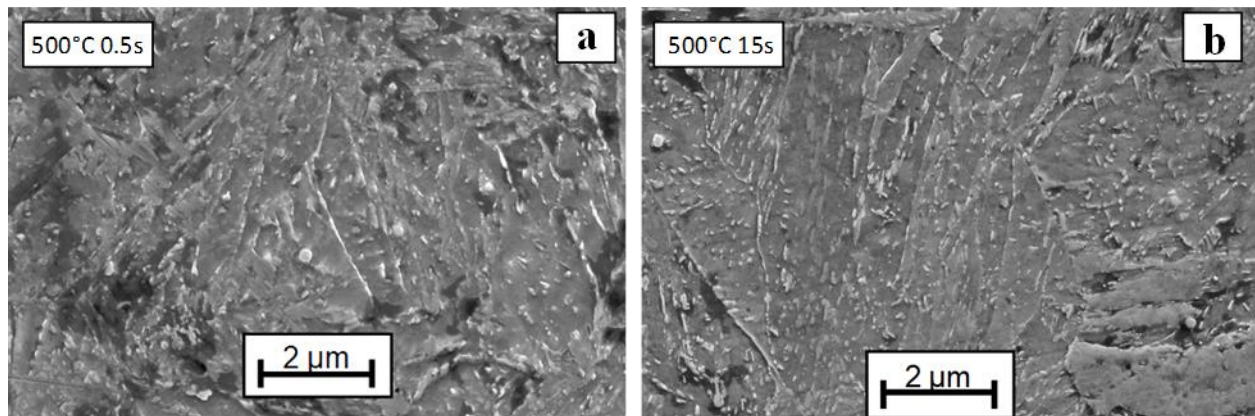


Figure 32: SEM micrographs of sample tempered at 500 °C for Steel A

The specimens tempered at 700°C had a mixed microstructure of martensite, ferrite and coarse precipitates. The specimen tempered for 0.5 s appears to retain more martensite, which can be seen in Figure 33 a. compared with the specimen tempered for 15 s which can be seen in Figure 33 b. Some small, spherical carbides can be seen which suggest cementite refinement at these higher temperatures, similar to what was observed by Sackl et. al [64]. Their work observed tempering heat treatments up to 700°C may be able to limit dislocation recovery. This reduction can provide increased nucleation sites for the formation of fine, dispersed cementite precipitates. Several very coarse irregular shaped carbides can also be observed within the microstructure of both samples. There are large band-like islands of martensite dispersed throughout the ferrite matrix in the

microstructure of the sample tempered for 0.5 s composed of many small cementite particles. There are some large carbide particles still visible in the ferrite matrix as well as long needle like martensite islands in a ferritic matrix [33]. The sample tempered for 15 s shows tempered martensite cementite particles in a range of sizes in a ferritic matrix.

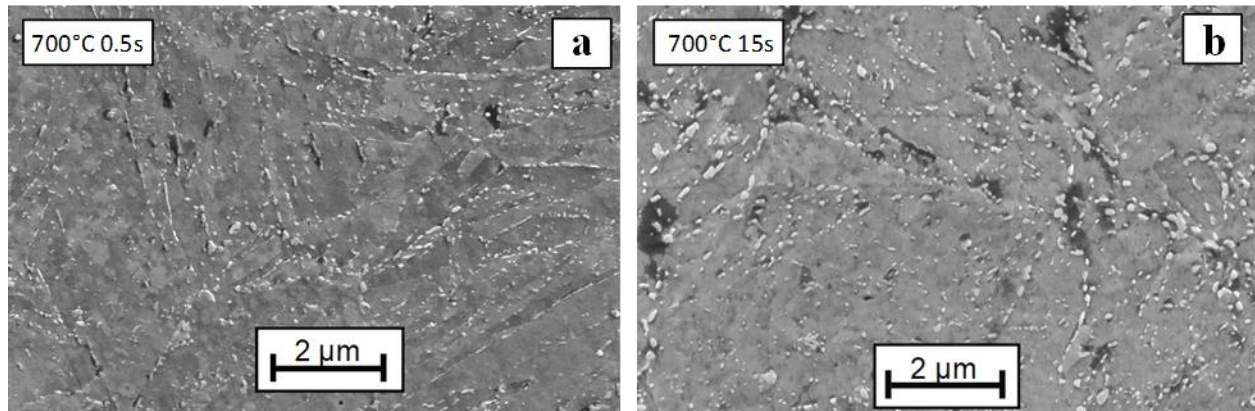


Figure 33: SEM micrographs of sample tempered at 700 °C for Steel A

3.2.2.2 Steel B Microstructural Results

Below are the resulting microstructures for the samples of Steel B tempered at 300, 500, and 700 °C and one fully hardened sample. The tempering times chosen for FE-SEM observation were 0.5s and 15s. The different tempering times and temperatures create a variety of resulting conditions in the final microstructures as shown for the 300-500-700 °C tempering conditions for both 0.5 and 15 s in Figure 35-Figure 37. In Figure 34 a micrograph of the fully hardened microstructure for Steel B can be seen. Each specimen of Steel B, before tempering, began with the microstructure of Figure 34. In Figure 34, some very large, coarse carbides can be seen in the lath martensite structure of this sample. But compared with the fully quenched microstructure of Figure 30, there are fewer of these very small carbides. Both fully austenized micrographs contain grains of very small carbides but the sample from Steel B shows smaller grains of these carbides than Steel A. The martensite of Steel B also has several areas of the very dense small carbides on the lath.

At tempering temperatures of 300 °C the observed microstructures for both hold times are, similar to Steel A, almost entirely martensitic. There are several very coarse carbides observable in the sample tempered for 0.5 s compared with the sample tempered for 15 s. The sample tempered for 15 s has many large grains of very fine, densely packed carbides which are not spherical. In contrast, the sample tempered for 0.5 s has much smaller pockets of these densely packed carbides, but these carbides appear even finer. There is also more lath martensite visible in the microstructure of the sample tempered for 0.5 s versus the one tempered for 15 s. The martensite appears to have begun to temper in Figure 35 b. compared with Figure 35 a. The hardness difference between the samples tempered for 0.5 and 15 s at 300 °C for Steel B are greater than that of Steel A. The softening at this temperature is already more distinct in the microstructures as well. The emergence of very large grains of slightly coarser carbides, and an increase in overall grain size may be contributing to the hardness difference. The coarsening of the carbides at this hold time is also apparent and also results in microstructure softening. The sample held for 0.5 s continues to retain larger areas of lath martensite as well as produce fewer carbides. There are some very coarse carbides visible, but the majority of the carbides observed were finer than those found in the samples held for 15 s. These observations occur at a very small time scale for the tempering temperatures.

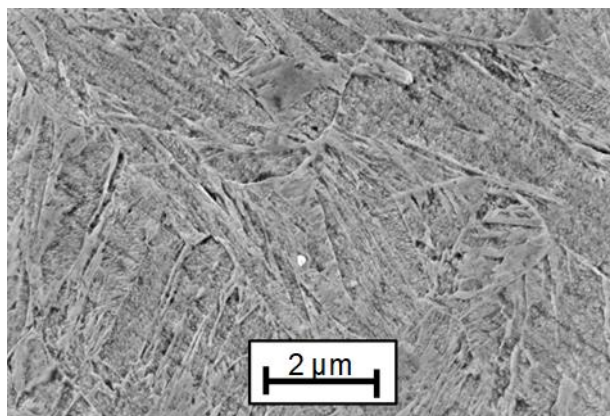


Figure 34: Fully quenched microstructure for Steel B

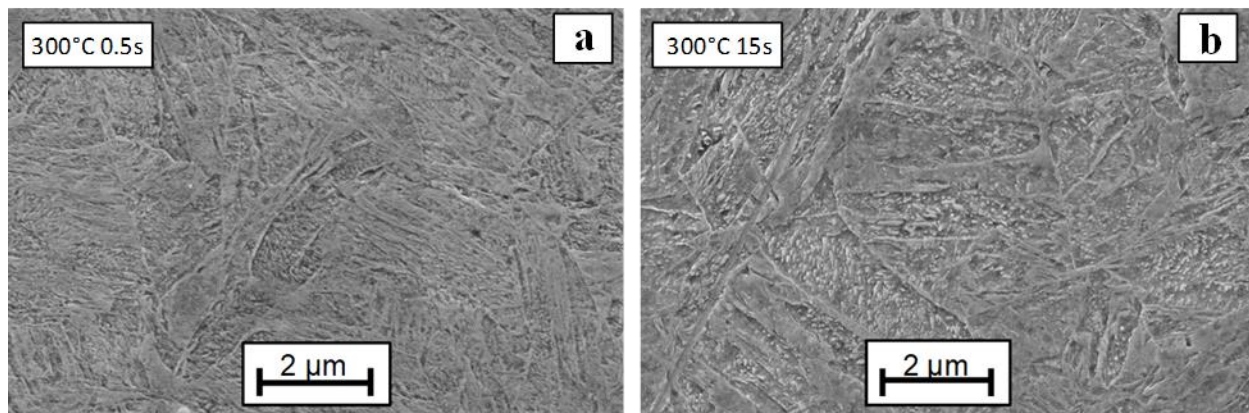


Figure 35: SEM micrographs of sample tempered at 300 °C for Steel B

The samples tempered at 500 °C for Steel B contain precipitates carbides and some martensite. This can be seen in Figure 36 a. and b. The carbides have begun to coarsen in both microstructures, but the amount of carbides visible in the specimen held for 0.5 s is greater than that of the specimen held for 15 s. The density of carbides is also higher in the sample held for 0.5 s compared with the 15 s. The 15 s hold also appears to contain more tempered martensite. Precipitation of carbides is likely to be complete at this temperature and the martensite has begun precipitating into cementite and ferrite. Areas of ferrite can be seen in both tempering conditions, but there is more observable ferrite in the specimens tempered for 15 s. The difference in hardness could be due to a large amount of carbides visible within the microstructure of the sample tempered for 0.5 s as well less martensite appears to have tempered in the samples held for 0.5 s.

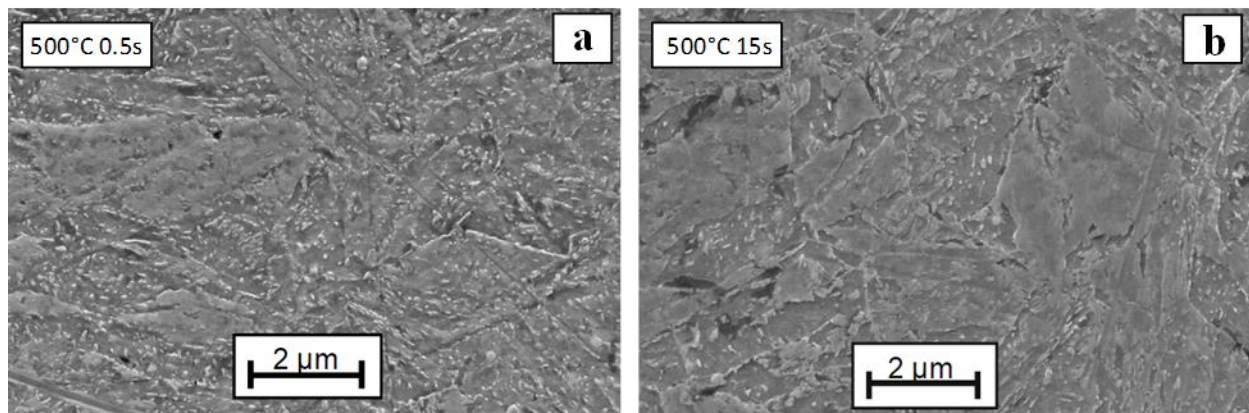


Figure 36: SEM micrographs of sample tempered at 500 °C for Steel B

The specimens tempered at 700 °C have a mixed microstructure of martensite, ferrite, and coarse carbides. The specimens tempered for 0.5 s and 15 s appear to contain similar amounts of carbides, which can be seen in Figure 37 a. and b. The carbides in both microstructures appear to be mainly irregular in shape. The carbides in the sample tempered for 0.5 s appear to be coarser than the ones tempered for 15 s. The carbides in the sample tempered for 15 s have likely coarsened due to the longer hold time. Some spherical carbides are visible in both microstructures, but not as many are visible compared to Steel A Figure 33 a. and b. The martensite in the sample held for 15 s appears to be more tempered than the sample held for 0.5 s. Both microstructures appear to have produced band-like islands of martensite dispersed throughout the ferrite matrix. The microstructure of the sample tempered for 15 s appears to have finer bands than the sample tempered for 0.5 s. The sample held for 0.5 s also shows some long, needle like martensite islands in the ferritic matrix.

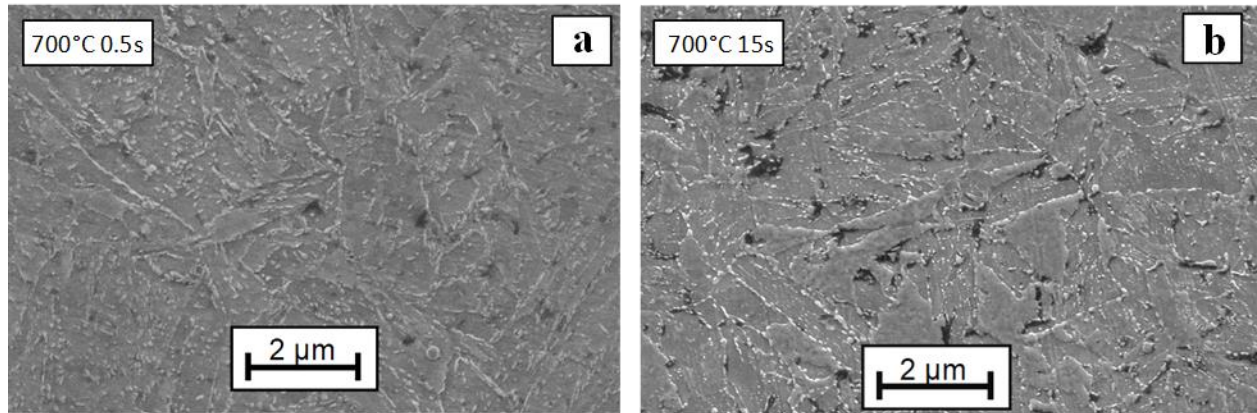


Figure 37: SEM micrographs of sample tempered at 700 °C for Steel B

4 Conclusions and Recommendations

4.1 Conclusions

In this study, two separate aspects related to press hardening of high carbon boron steels (steel A and B) were studied. In Part I, the austenite decomposition model used to simulate press hardening (FE model) was optimized using experimental data from constant cooling rate trials in which the final volume fractions of the resultant phases were quantified. Part II of this work investigated the effect of short cycle tempering on the softening and microstructural evolution of the fully hardened steels. Based on the finding presented, the following conclusions can be made from the results of this study.

4.1.1 Part I – Austenite Decomposition Model Optimization

- Gleeble tests were conducted on both 1800 MPa grade of boron steel and the quench conditions for TM1, TM2, 2.5, 5, and 10 °C/s resulted in mixed-phase microstructures consisting of ferrite, martensite, and bainite. A cooling rate of 50 °C/s both microstructures resulted in a fully martensitic microstructure.
- The resulting microstructure of Steel A was highly bainitic at critical cooling rates which allowed it to maintain high final hardness measurements compared with Steel B for TM1, TM2, 2.5, and 5 °C/s. These hardness differences between Steel A and Steel B were 78, 77, 33, and 42 HV for TM1, TM2, 2.5, and 5 °C/s respectively
- The resulting microstructure of Steel B for the sample quenched at 10 °C/s was mainly martensitic, unlike the sample created from the same quench rate for Steel A. This resulted in

a large hardness difference between the two of 155 HV. The resulting hardness between the samples of Steel A and B quenched at 50 °C/s resulted in higher hardness measurements for Steel B. The resulting hardness difference was found to be 10 HV.

- LS-Dyna was used to simulate the Gleeble tests for both steels and predict the phase transformations using the default model parameters and measured steel chemistry for the hot stamping material model *MAT_244. The result showed poor agreement with the measured as-quenched phases in both cases
- A simple optimization study was conducted and showed that an increased ferrite activation energy resulted in a more accurate prediction of the measured phases for all of the tests. The resulting optimization for Steel A proved more successful than Steel B. This may be due to the highest bainite content measured being found in the microstructure of the sample cooled at 5 °C/s, making convergence difficult to achieve between all percent errors.
- Due to the difference in hardness at the critical cooling rates, Steel A may be a better candidate for tailored die quenching.

4.1.2 Short Cycle Tempering

- The hardness of the as-quenched microstructure for both steels is significantly harder than the hardness of the microstructure tempered at 700 °C for all tempering times.
- There is a small increase in hardness for the samples tempered at 300 °C for 0.5, 1, and 2 s compared with the samples tempered for 300 °C for 5 and 15 s in Steel A. This may be due to the precipitation hardening effect.
- There is an increase in hardness for the samples tempered at 100 °C for 0.5, 1, 2, and 5 s compared with the samples tempered at the same temperature for 15 s in Steel B. This

may be due to the precipitation hardening affect.

- Steel B initially increases in hardness compared to Steel A before softening at similar rates for each temperature after 300 °C. At a tempering temperature of 600 °C, Steel B softens more than Steel A for tempering times of 15 s.
- The initial the microstructures of both steels for the samples tempered at lower temperatures are mainly martensitic with some finely dispersed carbides. The samples tempered for 0.5 s retain more fine carbides in the martensitic matrix, while the samples tempered for 15 s retain very little. The microstructure of the samples tempered at 700°C is a mix of martensite and ferrite, while the sample tempered for 0.5 s contain more martensite than the sample tempered for 15 s.

4.2 Future Work

To better understand the affect of critical quench rates and short cycle tempering on the resulting properties of both steels, the following recommendations should be considered for future work. For both experiments, mechanical testing must be performed to better understand the resulting strength of the material after heat treatment and conclude if the strength has been improved. For the short cycle tempering experiments, candidate tempering temperatures and times from the collected hardness data should be selected. V-bend and tensile specimens should be created at those tempering parameters for the purpose of deformation testing. A LS-Opt simulation should be used to further improve the LS-Dyna parameters for the quench rates and chemistries of Steel A and B. Improvements which can be made to the simulation of the phase decomposition of Steel B should be explored further. As well the CCT for both Steel A and B should be found to better understand the expression of phases in both materials during critical cooling.

REFERENCES

- [1] B. Behrens, A. Bouguecha, C. Gaebel, J. Moritz and J. Schrodter, "Hot Stamping of Load Adjusted Structural parts," *Procedia Engineering*, vol. 81, pp. 1756-1761, 2014.
- [2] H. Karbasian and A. E. Tekkaya, "A review of hot stamping," *Journal of Materials Processing Technology*, vol. 210, no. 15, pp. 2103-2118, 2010.
- [3] Plannja, "Manufacturing a hardened steel article". Sweden Patent GB1490535, 1977.
- [4] G. Berglund, "The History of Hardening of Boron Steel in Northern Sweden," in *1st International Conference on Hot Sheet Metal Forming of High-Performance Steel*, Kassel, 2008.
- [5] L. Garcia Aranda, Y. Chastel, J. Fernandez, T. Pascual and D. Negro, "Experiments and Simulations of Hot Stamping of Quenchable Steels," *Advanced Technology of Plasticity*, vol. 2, pp. 1135-1140, 2002.
- [6] K. Mori, P. Bariani, B.-A. Behrens, A. Brosius, S. Bruschi, T. Maeno, M. Merklein and J. Yanagimotoo, "Hot Stamping of Ultra-High Strength Steel parts," *CIRP Annals-Manufacturing Technology*, vol. 66, pp. 755-777, 2017.
- [7] W. D. Callister, Jr, *Materials science and engineering-an introduction*, New York: John Wiley & Sons, Inc, 2007.
- [8] R. Abbaschian, L. Abbaschian and R. E. Reed-Hill, *Physical Metallurgy Principles*, Toronto: Cengage, 2010.
- [9] A. International, *Practical Heat Treating*, 2nd Edition, Russel Township: ASM International, 2006.
- [10] M. Ali, D. Porter, J. Komi, M. Eissa, H. E. Faramawy and T. Mattar, "Effect of Cooling Rate and Composition on Microstructure and Mechanical Properties of Ultrahigh-Strength Steels," *Journal of Iron and Steel Research International*, pp. 1-16, 2019.
- [11] H. Jarvinen, M. Honkanen, O. Oja, M. Jarvenpaa and P. Peura, "Microstructure-Property Relationships of Novel Ultra-High-Strength Press Hardening Steels," *Metallurgical and Materials Transactions A*, vol. 50, no. 2, pp. 816-836, 2019.
- [12] H. Harbert, "Products in hot Stamped Boron Steel," *Capital Market Day*, 6 October 2015.
- [13] A. Tokizawa, K. Yamamoto and Y. Takemoto, "Development of 2000MPa class hot stamped steel components with good toughness and high resistance against delayed fracture," *4th*

International Conference on Hot Sheet Metal Forming of High-Performance Steel, vol. 4, pp. 456-472, 2013.

- [14] K. Hikida, T. Nishibata, H. Kikuchi, T. Suzuki and N. Nakayama, "Properties of New TS 1800 MPa Grade of Hot Stamping Steel and Application for Bumper Beam," *Proceedings of 4th International Conference on Hot Sheet Metal Forming of High-Performance Steel*, pp. 127-134, 2013.
- [15] H. Yi, P. Du and B. Wang, "A New Invention of Press-Hardened Steel Achieving 1880 MPa Tensile Strength Combined with 16% Elongation in Hot Stamped Parts," in *Proceedings of 5th International Conference on Hot Sheet Metal Forming of High-Performance Steel*, Toronto, 2015.
- [16] T. Taylor and J. McCulloch, "Effect of part/die boundary conditions on microstructural evolution during hot stamping 2000 MPa class boron steel," *Steel Research International*, vol. 89, no. 6, 2018.
- [17] M. Merklein, J. Lechler and T. Svec, "Deformation Dependent Conversion Behaviour of Press Hardened Boron Manganese Steels," *Proceedings of the 4th International Conference on Hot Sheet Metal Forming*, pp. 143-161, 2009.
- [18] A. Tekkaya, J. Allwood, P. Bariani, S. Bruschi, J. Cao, S. Gramlich, P. Groche, G. Hirt, T. Ishikawa, C. Lobbe, J. Lueg-Althoff, M. Merklein, W. Misiolek, M. Pietrzyk, R. Shivpuri and J. Yangimoto, "Metal Forming Beyond Shaping: Predicting and Setting Product Properties," *CIRP Annals- Manufacturing Technology*, vol. 64, no. 2, pp. 629-653, 2015.
- [19] A. Bardelcik, K. Ghavam, G. R and J. Worswick, "An Impact Model of a Hot Stamped Lab-Scale B-Pillar with Tailored Properties," *Proceedings of the 3rd International Conference on Hot Sheet Metal Forming of High-Performance Steel*, pp. 221-228, 2011.
- [20] W. Liang, L. Wang, Y. Liu and Y. Zhang, "Hot Stamping parts with Tailored Properties by Local Resistance Heating," *Procedia Engineering*, vol. 81, pp. 1731-1736, 2014.
- [21] K. Mori and Y. Okuda, "Tailor Die Quenching in Hot Stamping for Producing Ultra-High Strength Steel Formed Parts having Strength Distribution," *CIRP Annals- Manufacturing Technology*, vol. 59, pp. 291-294, 2010.
- [22] K. Mori, T. Maeno and K. Mongkolkaji, "Tailored Die Quenching of Steel parts Having Strength Distribution Using Bypass Resistance Heating in Hot Stamping," *Journal of Materials Processing Technology*, vol. 213, pp. 508-514, 2013.
- [23] M. Oldenburg and G. Lindkvist, "Tool Thermal Cycle Design for Manufacturing of Components with Tailored Material Properties," in *Proceedings of the 3rd International Conference on Hot Sheet Metal Forming of High-Performance Steel*, Kassel, 2011.

- [24] R. George, A. Bardelcik and M. Worswick, "Hot Forming of Boron Steels Using Heated and Cooled Tooling for Tailored Properties," *Journal of Materials Processing Technology*, vol. 212, pp. 2386-2399, 2012.
- [25] Y. Prajogo, K. Omer, A. Bardelcik, R. George, M. Worswick, N. Adam and D. Detwiler, "Development of a Hot Stamped Side Impact Beam and Axial Crush Member with Tailored Properties- Numerical Models," in *4th Interantional Conference of Hot Sheet Metal Forming of High-Performance Steel*, Lulea, 2013, pp. 15-22.
- [26] Y. Prajogo, "Hot Stamping of a Boron Steel Side Impact Beam with Tailored Flange Properties- Experiments and Numerical Simulations," University of Waterloo, Waterloo, 2015.
- [27] K. Omer, R. George, A. Bardelcik, M. Worswick, S. Malcolm and D. Detwiler, "Development of a hot stamped channel section with axially tailored properties – experiments and models," *International Journal of Material Forming*, vol. 11, no. 1, pp. 149-164, 2018.
- [28] N. Field, M. Di Ciano, A. Gerlich and K. Daun, "Tailoring by Direct Contact Heating During Hot Forming/ Die Quenching," *The Minerals, Metals & Materials Society*, vol. 50, pp. 3705-3717, 2019.
- [29] J. Kirkaldy and D. Venugopalan, "Prediction of microstructure and hardenability in low alloy steels," *International Conference of Phase Transformations in Ferrous Alloys*, pp. 125-148, 1983.
- [30] P. Akerstrom and M. Oldenburg, "Austenite decomposition during press hardening of a boron steel- Computer simulation and test," *Journal of Materials Processing Technology*, vol. 174, pp. 399-406, 2006.
- [31] A. Shapiro, "Using LS-Dyna to model hot stamping," USA, Livermore Software Technology Corporation, 2009, pp. 37-45.
- [32] Y. Cai, F. S. Halim, G. Li and S. Chen, "Hot stamping simulation and austenite decomposition modeling of an automobile cross member," *Procedia Engineering*, vol. 15, pp. 4902-4907, 2011.
- [33] A. Bardelcik, M. J. Worswick and M. A. Wells, "The influence of martensite, bainite and ferrite on the as-quenched constitutive response of simultaneously quenched and deformed boron steel- Experiments and model," *Materials and Design*, vol. 55, pp. 509-525, 2014.
- [34] D. Dengel, "Short-Time Tempering of Steel," *Haerterei Technsiche Mitteilungen*, vol. 39, p. 182, 1984.
- [35] L. E. Samuels, "Tempering of Martensite," *Metallographical Microstructural Analysis*, vol. 3, pp. 70-90, 2014.

- [36] G. Speich and W. Leslie, "Tempering of Steel," *Metallurgical Transactions*, vol. 3, no. 5, pp. 1043-1054, 1972.
- [37] D. Saha, E. Biro, A. Gerlich and N. Zhou, "Effects of tempering mode on structural changes of martensite," *Materials Science and Engineering A*, vol. 673, pp. 467-475, 2016.
- [38] E. Bonnevie, G. Ferriera, D. Kaplanb , A. Ikhlefa and J. Oraina, "Morphological aspects of martensite-austenite constituents in intercritical and coarse grain heat affected zones of structural steels," *Material Science and engineering*, vol. 285, pp. 352-358, 2004.
- [39] I. Tkalcec, S. Azcoitia, S. Crevoiserat and D. Mari, "Tempering Effects on a Martensitic High Carbon Steel," *Material Science and Engineering A* , pp. 352-356, 2004.
- [40] Y. Ju, A. Goodall, M. Strangwood and C. Davis, "Characterisation of precipitation and carbide coarsening in low carbon low alloy Q&T steels during the early stages of tempering," *Materials Science and Egnineering A*, vol. 738, pp. 174-189, 2018.
- [41] G. Miyamoto and T. Furuhashi, "Growth of cementite with alloy partitioning during tempering of martensite," *ISIJ International*, vol. 21, pp. 484-485, 2008.
- [42] S. Nayak, V. B. Hernandez and N. Zhou, "Effect of Chemistry on Nonisothermal Tempering and Softening of Dual-Phase Steels," *The Minerals, Metals & Materials Society*, vol. 42, pp. 3424-3248, 2011.
- [43] W. Zhou, H. Guo, X. Zhenjia, W. Xuemin and C. Shang, "High strength low-carbon alloyed steel with good ductility by combininig the retained austenite and nano-size precipitates," *Materials Science and Engineering A*, vol. 587, pp. 365-371, 2013.
- [44] G. Malakondaiah, M. Srinivas and P. Rao, "Ultrahigh-Strength Low-Alloy Steels with Enhanced Fracture Toughness," *Progress in Material Science*, vol. 42, no. 4, pp. 209-242, 1997.
- [45] J. Krawczyk, P. Bala and J. Pacyna, "The effect of carbide precipitate morphology on fracture toughness in low-tempered steels containing Ni," *Journal of Microscopy*, vol. 237, no. 3, pp. 411-415, 2010.
- [46] J. Guzman-Aguilera, C. Martinez-Gonzalez, V. Baltazar-Hernandez, S. Basak, S. Panda, M. Razmpoosh, A. Gerlich and Y. Zhou, "Influence of SC-HAZ microstructure on the mechanical behavior of Si-TRIP steel welds," *Materials Science and Engineering A*, vol. 718, pp. 216-227, 2018.
- [47] R. Misra, H. Nathani, J. Hartmann and F. Siciliano, "Microstructural evolution in a new 770 MPa hot rolled Nb-Ti microalloyed steel," *Materials Science and Engineeering A*, vol. 394, no. 1-2, pp. 339-352, 2005.

- [48] Y. Ohmori and I. Tamura, "Epsilon Carbide Precipitation during Tempering of Plain Carbon Martensite," *Metallurgical Transactions A*, vol. 23, no. 10, pp. 2737-2751, 1992.
- [49] X. Deng, T. Fu, J. Li, X. Li, Z. Wang and G. Wang, "Effect of epsilon carbides on mechanical properties and wear resistance of low alloy abrasion resistance steel," *The minerals, metals, and materials Society*, pp. 843-849, 2015.
- [50] H. Matsuda, R. Mizuno, Y. Funakawa, K. Seto, S. Matsuoka and Y. Tanaka, "Effects of auto-tempering behaviour of martensite on mechanical properties of ultra high strength steel sheets," *Journal of Alloys and Compounds*, vol. 577, pp. 661-667, 2012.
- [51] H. Jarvinen, M. Honkanen, M. Jarvenpaa and P. Peura, "Effect of paint baking treatment on the properties of press hardened boron," *Journal of Materials Processing Tech.*, vol. 252, pp. 90-104, 2018.
- [52] C. Sun, S. Liu, R. Misra, Q. Li and D. Li, "Influence of intercritical tempering temperature on impact toughness of a quenched and tempered medium-Mn steel: Intercritical tempering versus traditional tempering," *Materials Science & Engineering S*, vol. 711, pp. 484-491, 2018.
- [53] Y. Lu, A. Peer, T. Abke, M. Kimchi and W. Zhang, "Subcritical heat affected zone softening in hot-stamped boron steel during resistance spot welding," *Materials and Design*, vol. 155, pp. 170-184, 2018.
- [54] M. Xia, E. Biro, Z. Tian and N. Zhou, "Effects of heat input and martensite on HAZ softening in laser welding of dual phase steels," *ISIJ International*, vol. 48, no. 6, pp. 809-814, 2008.
- [55] V. Baltazar Hernandez, S. Nayak and N. Zhou, "Tempering of martensite in dual-phase steels and its effects on softening behaviour," *Metallurgical and Materials Transactions A*, vol. 42, no. 10, pp. 3115-3129, 2011.
- [56] J. Zhang, A. Khan, O. A. Ojo, N. Zhou and D. Chen, "Analysis of microstructural changes in the heat-affected zone and fusion zone of a fiber laser welded DP980 steel," *Metallurgical and Materials Transactions B*, vol. 4, no. 46, pp. 1638-1646, 2015.
- [57] H. Ghassemi-Armaki, E. Biro and S. Sadagopan, "Advanced characterization of HAZ softening of AHSS for crash modeling," *ISIJ International*, vol. 57, no. 8, pp. 1451-1460, 2017.
- [58] E. Biro, J. R. McDermid, S. Vignier and N. Zhou, "Decoupling of the softening processes during rapid tempering of a martensitic Steel," *Materials Science and Engineering A*, vol. 615, pp. 395-404, 2014.
- [59] S. Gunnardottir and A. Basurto, "Geometry Effects of Laser Tempering in Boron Steel Before Self-Pierce Riveting," Chalmers University of Technology, Gothenberg, 2015.

- [60] H. Kim, B. McAllister and S. Ream, "Laser Tempering for Crash Management," in *Great Designs in Steel 2016*, 2016.
- [61] O. Hedegard and M. Aslund, "Tempering of Hot-Formed Steel Using Induction Heating," Chalmers University of Technology, Gothenburg, 2011.
- [62] S. T. Ahn, D. S. Kim and W. J. Nam, "Microstructural evolution and mechanical properties of low alloy steel tempered by induction heating," *Journal of Materials Processing Technology*, vol. 160, pp. 54-58, 2004.
- [63] J. Lee, N. Kang, J. Park, S. Ahn, Y. Park, I. Choi, K. Kim and K. Cho, "Kinetics of Carbide Formation for Quenching and Tempering Steels During High-Frequency Induction Heat Treatment," *Materials Chemistry and Physics*, vol. 129, pp. 365-370, 2011.
- [64] S. Sackl, M. Zuber, H. Clemens and S. Primig, "Induction tempering vs. conventional tempering of a heat treatable steel," *The Minerals, Metals & Materials Society*, vol. 47, no. 7, pp. 3694-3702, 2016.
- [65] V. Judge, J. Speer, K. Clarke, K. Findley and A. Clarke, "Rapid Thermal Processing to Enhance Steel Toughness," *Scientific Report*, vol. 8, p. 445, 2018.
- [66] ASTM International, "ASTM E407-07(2015) e1 Standard Practice for Microetching Metals and Alloys," in *Conshohocken*, PA, 2015.
- [67] A. Bardelcik, C. J. Vowels and M. J. Worswick, "A mechanical, microstructural, and damage study of various tailor hot stamped material conditions consisting of martensite, bainite, ferrite, and pearlite," *Metallurgical and Materials Transactions A*, vol. 49, no. 4, pp. 1102-1120, 2018.
- [68] E. Biro, J. McDermid, S. Vignier and Y. Zhou, "Decoupling of the Softening Processes During Rapid Tempering of a Martensitic Steel," *Materials Science & Engineering A*, vol. 615, pp. 395-404, 2014.